Determining the Jet Energy Scale and Resolution of the Forward Calorimeters in the ATLAS Experiment at the Large Hadron Collider

Wesley Richard Clark Ernst

Master of Science

Department of Physics

McGill University

Montréal, Québec

2012-12-14

A THESIS SUBMITTED TO MCGILL UNIVERSITY IN PARTIAL FULFILMENT OF THE REQUIREMENTS FOR THE DEGREE OF MASTER OF SCIENCE

DEDICATION

I dedicate this work to Oren Wentworth Crowder and Ozwald Warren Nentwig.

ACKNOWLEDGEMENTS

First and foremost I thank God who has truly blessed me in my life. Special thanks go towards my supervisors Dr. Francois Corriveau and Dr. Brigitte Vachon who gave me the opportunity to work with the McGill ATLAS Group. I would like to thank Malachi Schram, Cibran Santamarina-Rios, Marc-André Dufour and Bertrand Chapleau for their invaluable help with computer programming problems and helping me find my way around the vast and treacherous ATLAS software infrastructure. Katie Woods, Rodger Mantifel, Michael Stoebe, Mike Collicutt, Yony Bresler, Robert Keyes and Michelle McKeown need to be thanked for they guided me when I was lost, grounded me when I was eccentric, cheered me up when I felt blue and motivated me when I felt lackadaisical. In short they kept me sane. I thank Aidan McCardle for connecting me to the world wide web at McMaster and Evan Rand for his friendship, constant support and proofreading skills. Final thanks go to my beloved parents, Rick and Linda Ernst and four siblings, Krista-lee, John, Chad and Katelyn. Their love, support and belief in me never ceases to amaze me. I love you all.

ABSTRACT

The jet energy scale and resolution of the forward calorimeters of the ATLAS detector are two important measurements for physics analyses dependent on missing transverse energy measurements and jet tagging efficiencies. This thesis investigates the validity of the current calibration or jet energy scale of the ATLAS forward calorimeters in the pseudorapidity region of $3.6 < |\eta| < 4.6$ using the di-jet balance method. The jet energy resolution is also investigated for this region using the same technique. This analysis was applied to the data collected from proton-proton collisions at a centre-of-mass energy of $\sqrt{s} = 7$ TeV in 2010, which corresponds to a total integrated luminosity of approximately 35 pb^{-1}. It is shown that the current jet energy scale is clearly not satisfactory and needs to be corrected. Correction factors for the jet energy scale are derived and shown to considerably improve the overall calibration. The jet energy resolution is also shown to have a stochastic term of $\left(180^{+38}_{-16}\right)\% \sqrt{\mathrm{GeV/c}}$ for 2−jet events and $\left(210^{+48}_{-71}\right)\% \sqrt{\mathrm{GeV/c}}$ for ≥ 3−jet events.

ABRÉGÉ

L'échelle en énergie des jets et la résolution en énergie des calorimètres vers l'avant du détecteur ATLAS constituent deux mesures importantes pour les analyses de physique qui dépendent de l'énergie transversale manquante et de l'efficacité d'identification des jets. Cette thèse étudie la validité de la présente calibration qui détermine l'échelle en énergie des calorimètres vers l'avant d'ATLAS dans la région de pseudorapidité $3.6< |\eta| < 4.6$ en utilisant la technique des balance des di-jets. La résolution en énergie des jets est aussi étudiée dans cette région en utilisant la même technique. Cette analyse est faite pour les données recueillies en 2010 pour des collisions proton-proton à une énergie du centre de masse de $\sqrt{s} = 7$ TeV, correspondant à une luminosité intégrée totale d'environ 35 pb^{-1}. Il y est démontré que l'échelle en energie des jets utilisée en ce moment est loin d'être satisfaisante et se doit dêtre corrigée. Les facteurs de correction pour l'échelle en énergie des jets sont donc calculés, démontrant une amélioration considérable de la calibration générale. La résolution en énergie des jets est alors déterminée, indiquant un terme stochastique de $\left(180^{+38}_{-16}\right)\%\sqrt{\mathrm{GeV/c}}$ pour les événements à 2−jets et $\left(210^{+48}_{-71}\right)\%\sqrt{\mathrm{GeV/c}}$ pour les événements à $\geq 3-$jets.

TABLE OF CONTENTS

LIST OF TABLES

LIST OF FIGURES

CHAPTER 1
Introduction

The completion and start-up of the Large Hadron Collider (LHC) at the European Organization for Nuclear Research (CERN) outside of Geneva, Switzerland in the spring of 2009 was a historic milestone for the scientific community. The LHC collides two counter-rotating beams of protons at unprecedented centre-of-mass energies in order to produce an environment similar to the universe a fraction of a second after the Big Bang [5]. The data collected from these high energy collisions are used to test the currently accepted model describing the most fundamental particles of the universe and their interactions. This model is called the *Standard Model of Particle Physics* or the "Standard Model" for short [6]. The ATLAS (A Toroidal LHC ApparatuS) detector [7] is one of two general purpose detectors on the LHC ring that are specifically designed to be sensitive to the various production modes and mass ranges of the Higgs particle.

1.1 Theoretical Motivation

The Standard Model has been developed over the last 45 years [8] in order to describe three out of the four forces in nature: electromagnetism, the weak force and the strong force. The gravitational force is the only force not described by the Standard Model. The Standard Model classifies the fundamental particles of matter into two groups, $\frac{1}{2}$ spin *fermions* and integer spin *bosons*. There are 12 fermionic particles which are categorized further into two groups of six particles called *leptons*

and *quarks*. These two groups are divided based on their electric charges and the forces through which they interact with one another. While leptons have integer electric charge and can interact via the electromagnetic and weak forces, quarks have only fractional electric charges and can interact via all three forces.

All fermions are point-like particles and each group has three doublet families or generations. Every fermion also has one antiparticle which differs only by an oppositely signed electric charge. The antiparticles associated with the neutral fermions differ by having an opposite chirality. The first generation of leptons and quarks constitute all of the visible stable matter in the Universe. Matter composed of the higher fermionic generations have much shorter life spans. Figure 1–1 shows each lepton and quark paired in their doublet families along with their respective masses, charges, and spins. Within the Standard Model, interactions are mediated by four types of gauge bosons which give rise to the three fundamental forces: electromagnetism, the weak force and the strong force.

The electromagnetic force acts between two charged particles and is mediated by the massless photon. The theory that governs this interaction is called Quantum Electrodynamics.The only particles unaffected by this force are the neutral leptons called neutrinos. The weak force is mediated by the $W^{\pm}$ and Z^0 bosons which have differing masses [10].

The gluon is the mediator of the strong force between (anti-)quarks and is described by Quantum Chromodynamics. A unique property of Quantum Chromodynamics is asymptotic freedom. Asymptotic freedom implies that the strength

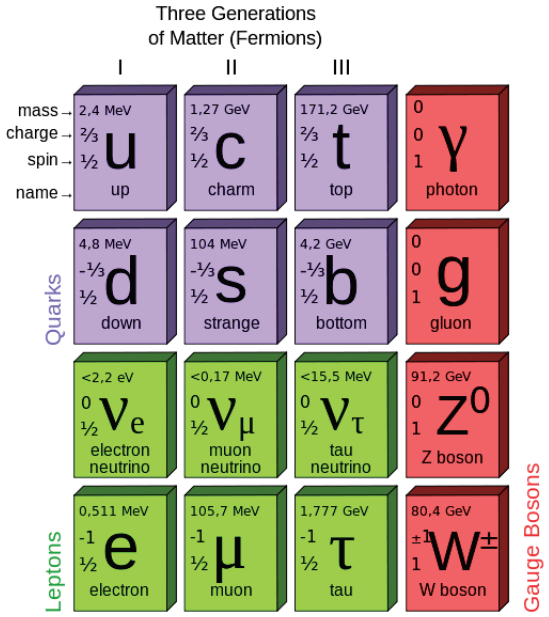

Figure 1–1: A visual description of the elementary particles in the Standard Model [9].

of the strong force approaches zero as the distance between the interacting particles decreases. Conversely the strength of the strong force increases with increasing distance between the interacting particles. Gluons and quarks also have a property analogous to the electric charge but unique to the strong force, called "colour" charge. Quantum Chromodynamics allows for three colour charges commonly referred to as "red", "green" and "blue". Each colour charge also has a respective anti-colour called "anti-red", "anti-green" and "anti-blue". Each (anti-)quark has one of three (anti-)colour charges whereas gluons carry two charges, one colour and one anticolour. A colour-anticolour pair or the sum of all three (anti-)colours forms a colourless charge. Colour charged particles like (anti-)quarks or gluons are not observed as free particles in nature but rather in colourless charge states. The phenomenon

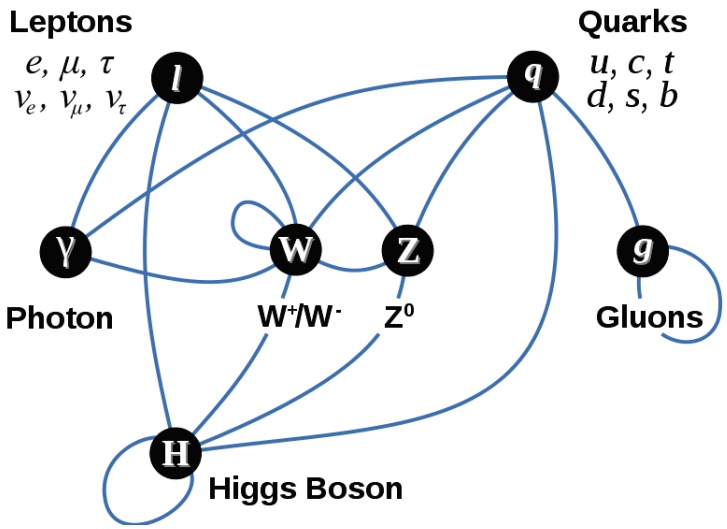

Figure 1–2: A visual description of how all the elementary particles in the Standard Model interact [11].

is called colour confinement. All particles consisting of quarks and antiquarks are called *hadrons*. Hadrons made of a quark-antiquark (colour-anticolour) bound state are called mesons, and hadrons consisting of a 3-quark bound state (all three (anti-)colours) are called baryons. Figure 1–2 is a visual representation of all the possible interactions between the fundamental particles discussed above.

1.2 Jet Production

Colour confinement prevents the detection of single isolated quarks or gluons in nature or after high energy hadron collisions like those occurring at the LHC. During these high energy collisions, partons (quarks and/or gluons) are ejected or created from the original hadrons. When partons are bound together forming a hadron, they interact freely with themselves and others through the emission and absorption of gluons. However when a quark is ejected from a hadron, the energy of the gluon connecting the two particles increases to the point where it breaks and spontaneously

creates a quark-antiquark pair. This process is called *hadronization*. The "new" emitted hadron then radiates gluons creating a collimated spray of particles commonly referred to as a *jet*.

A visual representation of the evolution of a jet is shown in Figure 1–3. The evolution of a jet can be separated into three parts: parton, particle and calorimeter jets [12]. At the parton level, ejected partons undergo *fragmentation* where gluons are radiated. This is analogous to how electrically charged particles radiate photons when accelerated, a process known as bremsstrahlung. Following from this, a spray of partons or parton cascade is created, called the parton level jet. The parton level jet quickly undergoes hadronization, transforming the cascade into a particle level jet. It should be noted that electromagnetic particles do not go through fragmentation or hadronization. The final step in the evolution of a jet occurs when the collimated spray of particles within the particle jet interacts with the detector and deposits its energy within. Detectors that are specifically designed to detect such energy deposits are called *calorimeters*. The energy deposits are then found and grouped together to form calorimeter level jets, which are discussed in further detail in Chapter 3. The

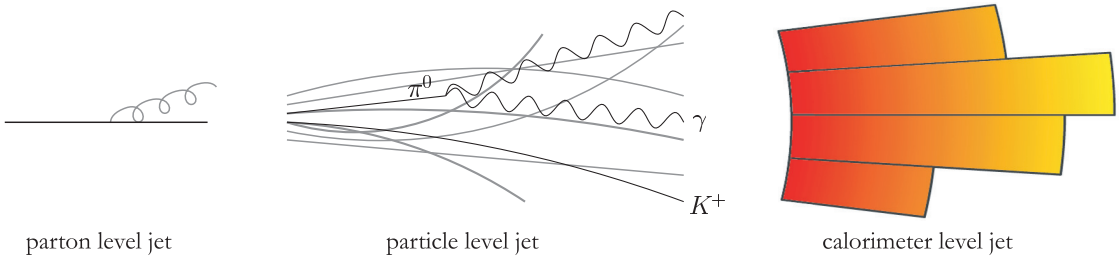

Figure 1–3: A depiction of the evolution of a jet [12].

next section briefly discusses particle interactions within matter and two different types of showering processes.

1.3 Showering Processes

Calorimetry refers to the total absorption of particles within a set volume of matter (calorimeter) in order to measure their total energy. Particles deposit their energy through different fundamental physics interactions based on their type. Particles with sufficient energy can produce cascades of secondary particles called *showers*. There are two types of showers, electromagnetic and hadronic depending on the type of the incident particle.

1.3.1 Electromagnetic Showers

Charged particles such as the electrons and positrons interact with matter via two primary processes: ionization/excitation of atomic electrons and Bremsstrahlung [13]. Other processes such as Bhabba and Møller scattering and electron-positron annihilation occur as well but are negligible in comparison for the energy region considered at the LHC. Atom ionization and excitation occurs when an incident electron[1] strikes an atom and causes the ejection or excitation of one of the orbital electrons. These are the dominant energy loss processes in matter for electrons/positrons with energies below the critical energy E_C given by [10, 14],

$$E_C \approx 550 \text{ MeV/Z}. \tag{1.1}$$

where Z is the atomic number of the material.

[1] Electrons and positrons are used interchangeably within this section.

For electron energies above E_C the dominant energy loss process is Bremsstrahlung. Bremsstrahlung occurs when an electron interacts with the Coulomb field of a nucleus causing it to accelerate (deflect) and emit a photon. At high electron energies a cone of highly collimated Bremsstrahlung photons is produced.

Photons interact with matter via three processes: the photoelectric effect, Compton scattering and pair production [13]. Figure 1–4 illustrates the dominant interaction processes for different incident photon energies and Z, of the absorber. The dominant interaction at low energies is the photoelectric effect where the absorption of the incident photon leads to the ejection of an electron from an atom. Therefore the binding energy of an electron in the atom sets a lower limit on the energy of the incident photon required for this process. The dominant energy loss process for photon energies from $\sim$1 to 10 MeV is Compton scattering. Compton scattering is the process by which incident photons are elastically scattered off of atomic electrons. This results in a decrease in photon energy and the ejection of the recoiling atomic electron.

For photon energies in the regime of particle colliders (GeV or TeV range), pair production is the primary interaction process. Pair production is the process by which a photon with an energy of at least $2m_ec^2 \approx 1022$ keV, interacts with a nucleus and is converted into an electron-positron pair.

Electromagnetic showers are produced at high energies where the dominant interactions of electrons and photons with matter are Bremsstrahlung and pair production respectively. The high energy photons produced via Bremsstrahlung produce electron-positron pairs which then produce more Bremsstrahlung photons. This

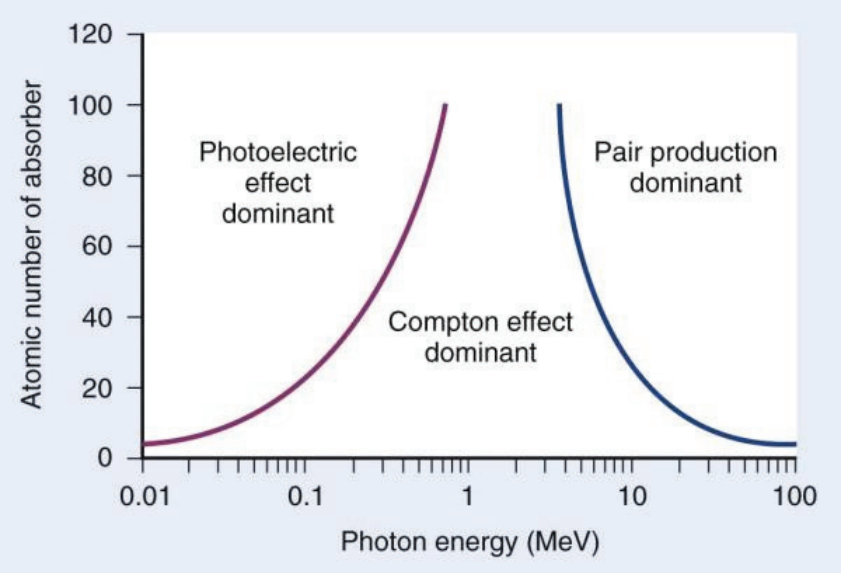

Figure 1–4: A depiction of the incident photon energy and atomic number of the absorber phase space where each of the photon interaction processes dominates [15].

chain-reaction progresses until the energy of the photons, electrons and positrons falls below the critical energy, E_C. Once below the critical energy, the photons undergo Compton scattering and photoelectric interaction whereas the electrons cease to radiate, losing the rest of their energy through atomic collisions. The depth at which a particle shower will penetrate the calorimeter is dependent on the energy of the incident particle and the atomic number of the calorimeter material. The development of an electromagnetic shower can be characterized by *radiation lengths*. A radiation length, X_0, is defined to be the length that a high energy electron must travel to lose $1/e$ of its energy via Bremsstrahlung [10].

1.3.2 Hadronic Showers

High energy hadrons typically interact with matter through inelastic nuclear processes by which nuclei are excited or broken apart (spallation) into multiple secondary

particles. These secondary particles in turn, interact with the material creating a hadronic shower of particles. Hadronic showers continue through the material until the particles do not have enough energy to break apart the nuclei. At this point the particles are absorbed through nuclear processes. The longitudinal hadronic shower depth can be characterized by a nuclear interaction length, λ_{int}. The nuclear interaction length is defined as the average distance a hadron travels in matter before interacting with a nucleus and is much larger than the radiation length. Therefore hadronic showers have the potential to penetrate deeper into the detector material than electromagnetic showers.

Hadronic showers also typically produce electromagnetic particles which deposit their energies via electromagnetic processes. For example, neutral pions, π^0, are produced in hadronic showers which readily decay into two photons. Provided the photons have enough energy, they can produce an electromagnetic shower within the hadronic shower. On average, neutral pion production causes one third of the hadronic shower to be electromagnetic, however this may fluctuate greatly.

1.4 Calorimetry

All of the ATLAS calorimeters are *sampling calorimeters*. Sampling calorimeters are made of alternating active and passive layers of material. The ATLAS calorimeter system is designed such that hadronic calorimeters are placed further from the collision point behind electromagnetic calorimeters. Hadronic calorimeters are usually designed to have a short nuclear interaction length in order to fully contain any hadronic particle showers. Electromagnetic calorimeters are designed to provide accurate energy measurements for electrons, positrons and photons as well as contain

most of any electromagnetic particle showers. The active layers of the calorimeter are where the energy measurements are made, thus only a fraction of the total energy deposited in the calorimeter is actually measured. The passive layers are usually composed of elements with high atomic numbers and are used to promote shower development as well as ensure that the shower is fully contained.

1.4.1 Compensation

The energy response of a calorimeter for a particular particle is defined by $E_{measured}/E_{actual}$ where $E_{measured}$ is the measured energy and E_{actual} is the actual energy of the particle. The energy response for electromagnetic (e) and hadronic (h) particles for a given calorimeter can be characterized by the ratio e/h, and may vary depending on the material with which the calorimeter was constructed. Compensation is the act of obtaining the same energy response for electromagnetic and hadronic particles within a given calorimeter or $e/h = 1$. Compensation is desirable because it can improve the performance of the calorimeter, namely the energy resolution during data acquisition [16].

The precision to which a calorimeter can measure the energy of a particle (hadronic or electromagnetic) is referred to as its energy resolution. The dependence of the energy resolution of a calorimeter on the ratio e/h is given by [17],

$$\frac{\sigma\left(E\right)}{E} \propto \frac{k_1}{\sqrt{E}} + k_2 \cdot |e/h - 1| \tag{1.2}$$

with $k_i > 0$. Therefore when a calorimeter is well compensated ($e/h = 1$) the second term in Equation 1.2 vanishes which improves the energy resolution.

One way to achieve compensation is to carefully choose the calorimeter material in order to decrease e and increase h; however this can lead to overcompensation. Most calorimeters are non-compensating, meaning that they do not measure all of the hadronic energy deposited and have $e/h > 1$. Offline software is used in order to adjust the calorimeters response to a ratio of $e/h = 1$. All of the ATLAS calorimeters are non-compensating and are calibrated to the electromagnetic energy scale. This means that every calorimeter signal, electromagnetic and hadronic, has an initial calibration applied such that $e = 1$. This is accomplished through rigorous studies involving simulated and test beam data [18]. Once the showers have been reconstructed into jets an additional calibration called the jet energy scale is also applied to account for energy deposited by hadrons as well as any unrecorded energy deposits due to detector abnormalities.

Unlike test beam data where the particle type and energy can be known, the particles created from the proton-proton collisions at the ATLAS detector are not. The ATLAS calorimeter system is heavily relied upon in order to sort through and organize the data collected. The jets found within the calorimeters after a collision are approximations of the energy and direction of the particles which created the showers. The accuracy to which the calorimeters can properly reconstruct a jet's energy is referred to as the jet energy resolution.

This masters thesis determines the jet energy scale and resolution of a part of the calorimeter system of the ATLAS detector. Chapter 2 presents an overview of the LHC as well as a brief descriptions of the ATLAS detector subsystems. Chapter 3 discusses jets within the ATLAS detector including their reconstruction, calibration

and resolution. Chapter 4 gives a detailed outline of the technique used to deduce the jet energy scale and resolution. Finally, Chapters 5 and 6 present the results and conclusions of the analysis, respectively.

CHAPTER 2
Experimental Description

2.1 The Large Hadron Collider

The LHC straddles the France-Switzerland border lying within the old, circular Large Electron-Positron collider tunnel ranging from 50 to 150 metres in depth and a circumference of ∼27 km.

The LHC has successfully accelerated and collided two counter-rotating proton beams to a centre-of-mass collision energy of 7 TeV[1] . This energy is about three times larger than that of the former Tevatron collider located outside of Chicago, Illinois [20]. Along the beam pipe, approximately 1232 superconducting dipole and 600 quadrupole magnets are used to bend and stabilize each proton beam. The LHC is also equipped to accelerate and collide heavy ions such as lead at centre-of-mass energies up to 5.5 TeV per nucleon-nucleon collision. The proton beams are not composed of a steady stream of protons but in fact are made of periodic groups of protons called *bunches*. The bunches are separated from one another by ∼25 ns and have an average of 10^{11} protons in each bunch[2] . Each proton beam travels through five intermediate accelerators before reaching its desired collision energy. Figure 2–1

[1] The design centre-of-mass energy is 14 TeV.

[2] The actual bunch separation in the collisions in 2010 was 50 ns.

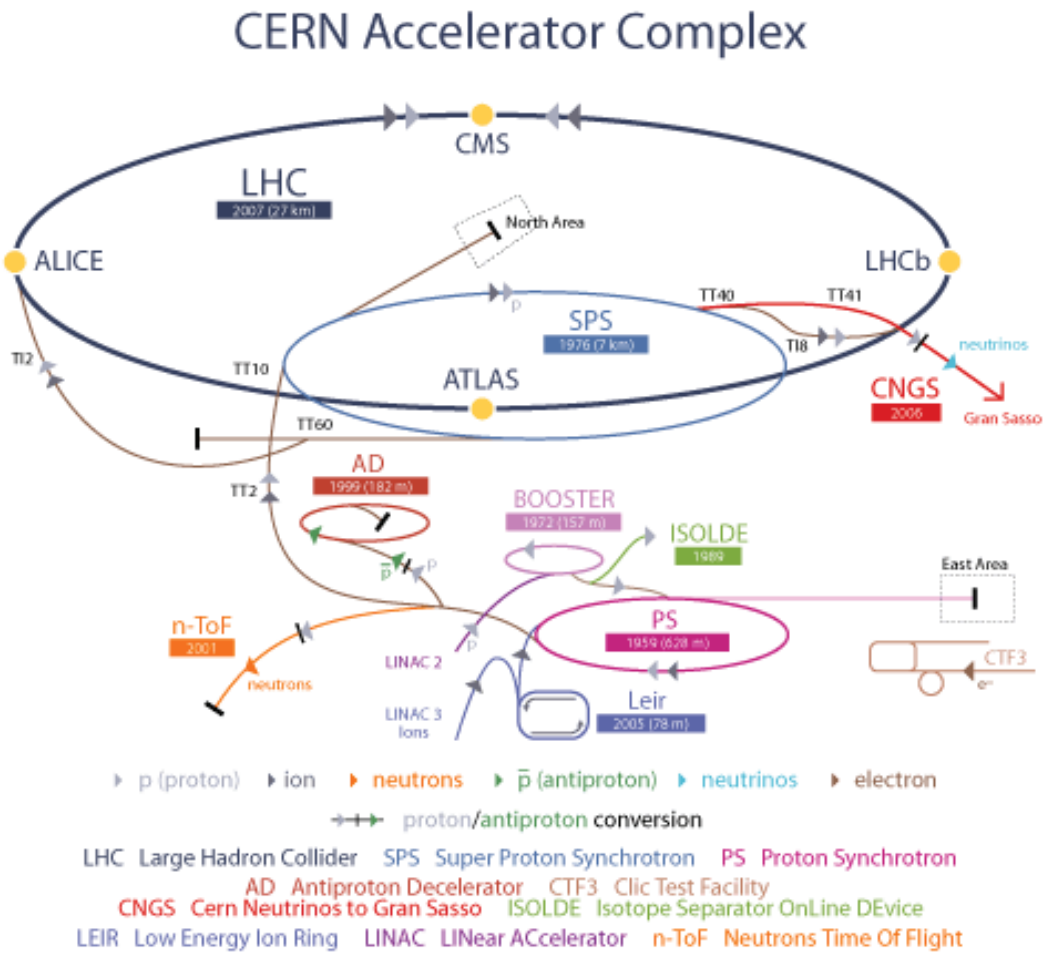

Figure 2–1: A general overview of the LHC accelerator complex [19].

shows these five accelerators which make up the LHC accelerator complex. Each accelerator uses a series of radio frequency cavities to accelerate the charged bunches of particles [21]. Protons are first accelerated by a linear accelerator to an energy of 50 MeV before being injected into the Proton Synchrotron Booster. The Proton Synchrotron Booster then accelerates the proton bunches to an energy of 1.4 GeV before injecting them into the Proton Synchrotron for further acceleration up to

an energy of 25 GeV. The bunches are then injected from the Proton Synchrotron into the Super Proton Synchrotron where they are accelerated to an energy of 450 GeV before being injected into the LHC ring. Finally the LHC ring accelerates the bunches to their final collision energies. This procedure is done for each counter-rotating proton beam.

At the collision point of the ATLAS detector the two proton beams are squeezed into a point of the order of 20 μm which yields luminosities up to a design luminosity of 10^{34} cm^{-2}s^{-1} [7]. In particle physics, luminosity refers to the measurement of the rate of interactions per unit area and can be instantaneous (luminosity at a moment in time) or integrated over a period of time (integrated luminosity). At the design luminosity, collisions between the highly populated proton bunches create on average 23 direct proton-proton or hard scattering collisions per bunch crossing at a rate of about 40 MHz. The detector information obtained at each bunch crossing is referred to as an event.

2.2 The ATLAS Detector

The ATLAS detector shown in Figure 2–2, stands 25 m tall, 44 m long and weighs ~7000 tonnes. Before continuing with the experimental overview, the coordinate system and some of the nomenclature associated with the ATLAS detector are defined.

The ATLAS detector uses a right-handed x-y-z coordinate system with the positive x-axis pointing toward the centre of the LHC ring, the positive y-axis pointing toward the sky and the z-axis along the beamline. The two beamlines cross at the

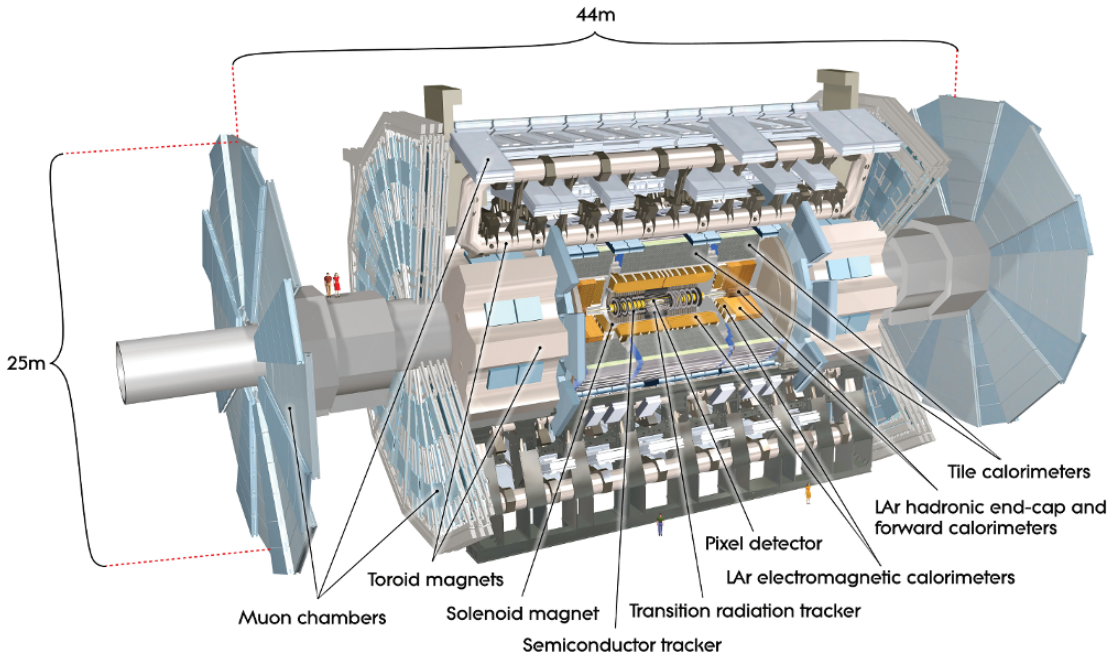

Figure 2–2: A longitudinal cross-section of the ATLAS detector [22].

$z = 0$ point which bisects the detector into Side A ($z > 0$) and Side B ($z < 0$). Definitions of some of the variables that will be used throughout this thesis include:

- Transverse measurements such as missing transverse energy E_T^{miss} are often used and are defined as the x and y contributions summed in quadrature. For example transverse momentum, p_T, is defined as,

$$p_T = \sqrt{(p_x)^2 + (p_y)^2} \tag{2.1}$$

  where p_x and p_y are the components of momentum in the x and y directions, respectively.

- ϕ is the azimuthal angle around the beam in the $x - y$ plane where

$$\tan\phi \equiv p_y/p_x \tag{2.2}$$

- θ is the polar angle measured from the $+z$ axis.
- Pseudorapidity[3] is defined as

$$\eta = -\ln\tan(\theta/2) \tag{2.3}$$

- The distance ΔR in the pseudorapidity-azimuthal angle plane is

$$\Delta R = \sqrt{\Delta^2\eta + \Delta^2\phi} \tag{2.4}$$

The ATLAS detector was designed to be able to identify the products of proton-proton collisions well enough to be sensitive to a broad range of physics within and beyond the Standard Model. The following criteria were laid out to achieve such physics goals [25]:

- Large pseudorapidity acceptance and full azimuthal angle coverage.
- Excellent electromagnetic calorimetry to efficiently identify and measure electrons and photons.
- Efficient tracking at high and low luminosities for charged particle identification and momentum measurements.
- Full angular coverage for hadronic calorimetry in order to make accurate missing transverse energy and jet measurements.

[3] Pseudorapidity is commonly used at hadron colliders because unlike regular rapidity, $y \equiv (1/2)\ln[(E+p_z)/(E-p_z)]$, it only depends on the measurement of the angular polar angle of a particle's trajectory [23, 24].

- A muon detection system that is completely independent of the rest of the detector with the capability of making extremely precise muon momentum measurements at high luminosities.
- Ability to measure and trigger on low transverse momentum particles to maintain sensitivity to as many physics processes as possible.

As a result of the criteria laid out above, the ATLAS detector was designed with five major components: the inner detector, magnet system, calorimeter detectors, muon detectors, and trigger/data acquisition systems.

The following sections will briefly discuss these components in the order stated above. A more detailed description can be found in the ATLAS detector paper in the Journal of Instrumentation [7]. The last section of this chapter will discuss in detail the forward calorimeter system as it is particularly relevant for the work presented in this thesis.

2.2.1 Inner Detector

The goal of the inner detector [7] shown in Figure 2–3 is to accurately measure the trajectory of charged particles. A 7 m long solenoidal magnet at a 1.15 m radius from the beamline immerses the inner detector in a 2 T magnetic field. This causes the trajectories of charged particles to be bent, which in turn allows for the determination of the momentum and sign of the charged particle. There are three components which make up the inner detector: the pixel detector, the silicon microstrip detector, and the transition radiation (TR) detector.

The pixel detector is comprised of 3 layers of radiation hard semi-conductor pixel detectors, increasing the ability of the inner detector to identify short-lived particles

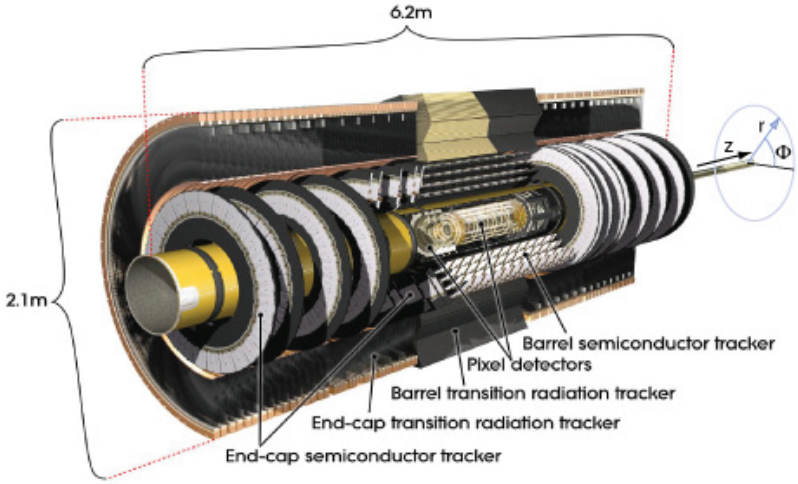

Figure 2–3: A longitudinal cross-section of the ATLAS inner detector [26].

including τ-leptons and b-quark hadrons. The silicon micro-strip detector works in conjunction with the pixel detector to provide good particle pattern recognition, momentum measurements and vertexing[4] . The outermost component of the inner detector is the TR tracker [27] with straw trackers. It consists of approximately 50000 axial and 320000 radial straw tube detectors in the barrel and end-cap regions, respectively. Each straw tube is filled with gas mixture consisting of 70% xenon (Xe), 27% carbon dioxide (CO_2) and 3% oxygen (O_2) and has a 30 μm diameter, gold plated tungsten-rhenium sense wire through its centre [28]. The straw tubes are within a matrix of 19 μm polypropylene fibres which serve as the transition radiation material. As electrically charged particles traverse the polypropylene fibres, TR photons are

[4] Vertexing is the act of reconstructing the parameters of an interaction or decay point (vertex) by using the trajectories and information from the outgoing particles produced.

produced which then ionize the Xe-CO_2-O_2 gas mixture within each straw tube. The ions then drift towards the sense wire creating a current which is read out. Since electrons produce more TR photons than pions, the TR tracker can also help distinguish between the two particles.

2.2.2 Magnet System

The magnet system [7] illustrated in Figure 2–4, consists of two end-cap toroids, a barrel toroid and a central solenoid, all of which are superconducting. The purpose of the magnet system is to bend the trajectory of charged particles' in order to determine the sign of the particles electric charge as well as its momentum. The configuration of each magnet provides a field orthogonal to most particle trajectories over a large η range. As discussed in Section 2.2.1, the central solenoid surrounds the inner detector. The barrel and end-cap toroids provide a magnetic field for an η range of $|\eta| < 2.7$ required for the muon spectrometer system. The peak field strengths for the barrel and end-cap toroids are 2 T and 4 to 8 T respectively. Each of the end-cap toroids consist of eight coils linked together creating a single cold mass housed in a large cryostat The end-caps are aligned with the central solenoid and are on rails to allow access to the detector for maintenance. The barrel toroid is comprised of eight coils housed in individual cryostats in a racetrack configuration measuring 25 m long and 5 m in width. There is eight-fold azimuthal symmetry in each of the toroidal magnet systems. Each end-cap toroid is rotated by 22.5 ° in ϕ with respect to the barrel toroid to provide a more uniform field to bend energetic electrically charged particles.

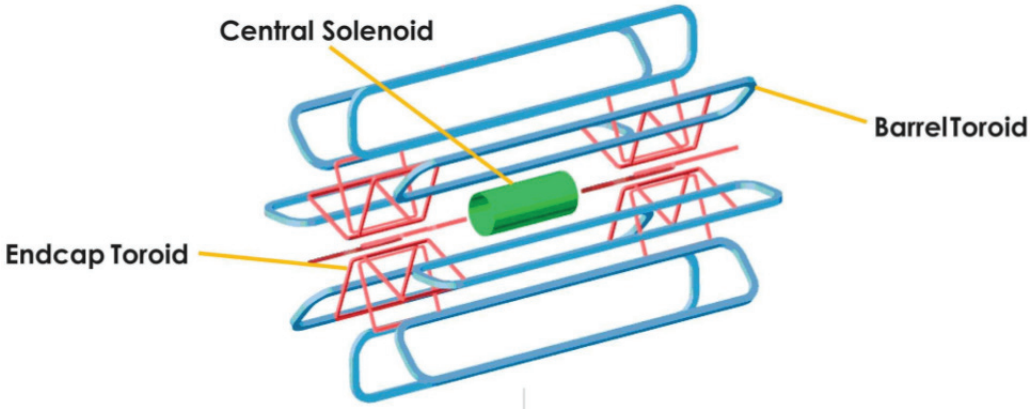

Figure 2–4: The arrangement of the ATLAS magnet system [29].

2.2.3 Calorimeters

The ATLAS calorimeter system [7] shown in Figure 2–5 has a full $|\eta|<$ 4.9 coverage and captures most of the particles produced at the interaction point. The ATLAS calorimeter design utilizes four different techniques to achieve the physics goals of the experiment and to meet the challenges that the harsh LHC environment poses. Since different types of particles interact with material differently, the ATLAS calorimeter system is split into an electromagnetic part and an hadronic part.

The two types of active layers that are used in ATLAS are liquid argon gaps and plastic scintillating tiles. When charged particles created in electromagnetic and hadronic showers traverse the liquid argon calorimeters, they ionize the liquid argon and produce an ionization current[5] . By measuring the ionization current the incident energy of the the charged particles can be determined. Charged particles

[5] Current induced by the liquid argon ions drifting to the anode or cathode depending on their charge

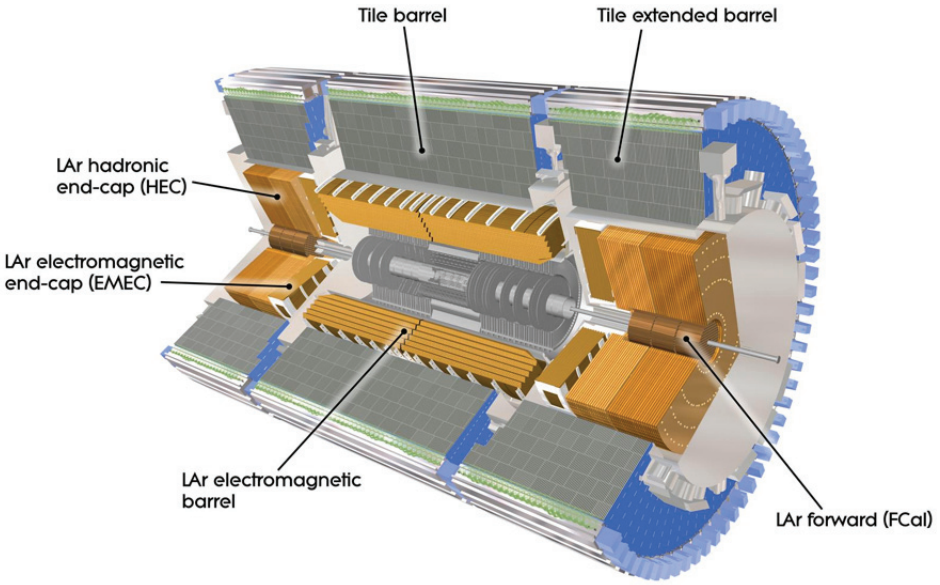

Figure 2–5: A longitudinal cross-section of the ATLAS calorimeter system [30].

passing through the tile calorimeters however, produce ultraviolet light which is then read out with wavelength shifting fibres and photomultiplier tubes. Each component of the calorimeter system will be briefly discussed in the next few sections.

The Electromagnetic Calorimeters

The electromagnetic calorimeters are divided into four parts, two identical half-barrel components separated by a small gap at z=0 ($|\eta|<1.475$) and two end-caps ($1.375<|\eta|<3.2$). A cut-away view of the electromagnetic barrel is shown in Figure 2–6. It is made of lead and liquid argon as the passive and active materials, respectively. The electrodes are laid out in an accordion-shape to remove the possibility of any azimuthal (ϕ) cracks. Unlike their barrel counterparts, each end-cap is divided into two coaxial wheels with the outer and inner wheels covering $1.375 < |\eta| < 2.5$

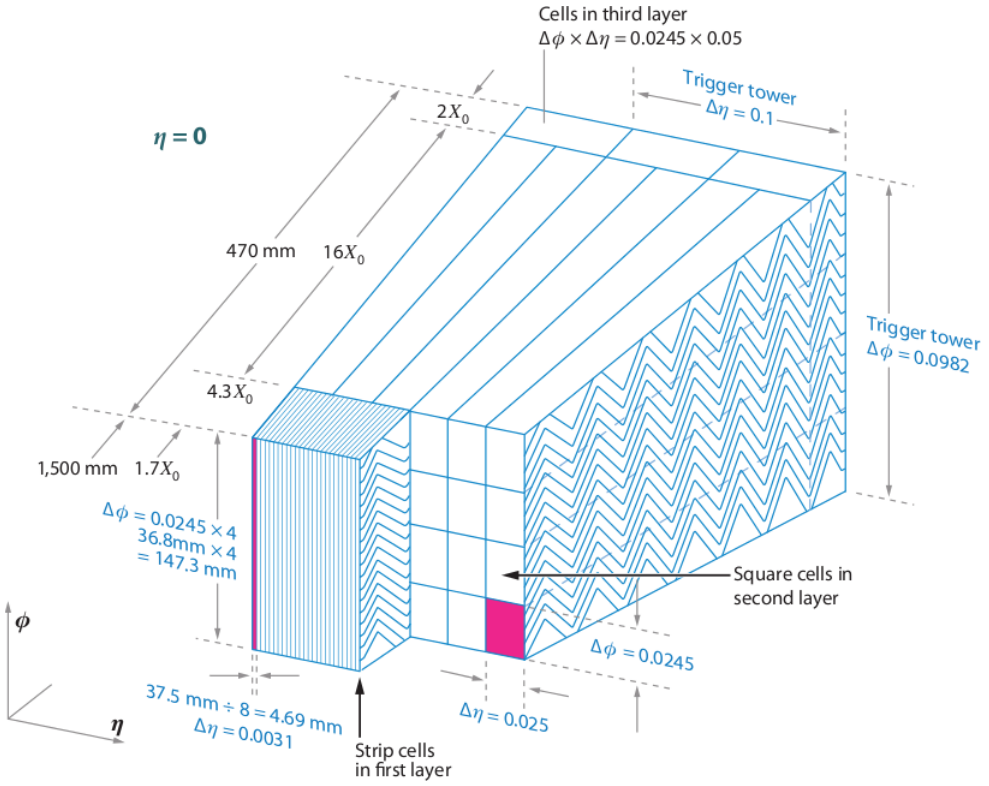

Figure 2–6: A cut-away view of the ATLAS Electromagnetic Barrel Calorimeter [31].

and $2.5 < |\eta| < 3.2$ respectively. The barrel end-cap calorimeters use copper as their passive material. In addition to the barrel and end-cap electromagnetic calorimeters, there is a presampler consisting of an active liquid argon layer of thickness 1.1 cm in the barrel region and 0.5 cm in the end-cap region. The presampler corrects for energy lost by electrons and photons upstream or towards the ends of the detector within $|\eta| < 1.8$. The electromagnetic barrel and end-cap calorimeters have expected energy resolutions of 10-17%/$\sqrt{E}\oplus$ 0.7% [7].

The Hadronic Barrel Calorimeters

The hadronic barrel calorimeter is made of plastic scintillating tiles and iron as the active and passive materials respectively. It is divided into a central barrel ($|\eta| < 1.0$) and 2 extended barrel ($0.8 < |\eta| < 1.7$) pieces. The barrel and extended barrel segments are separated by vertical gap approximately 68 cm wide which allows for inner detector read-out cables, service pipes for the electromagnetic calorimeter and the central solenoid, and houses front-end electronics for the electromagnetic calorimeter [7]. The expected resolution for this part of the calorimeter system is $50\%/\sqrt{E} \oplus 3\%$ [7].

The Hadronic End-Cap Calorimeters

The hadronic end-cap calorimeters are located right behind the electromagnetic end-cap calorimeters. They have liquid argon and copper as their active and passive material respectively. Each hadronic end-cap has an inner and outer wheel differing only by the thickness of the copper absorbers between passive material gaps. Both wheels have 8.5 mm gaps between consecutive copper plates which have three electrodes separating the gap into four drift spaces ~ 1.8 mm wide. Like the hadronic barrel calorimeters, the hadronic end-cap calorimeters have an expected energy resolution of $50\%/\sqrt{E} \oplus 3\%$ [7].

2.2.4 Muon Spectrometer

The primary goal for the muon spectrometer [7] depicted in Figure 2–7, is to provide accurate momentum and tracking measurements of muons. The muon spectrometer is constructed on the outside of the calorimeter system because muons are

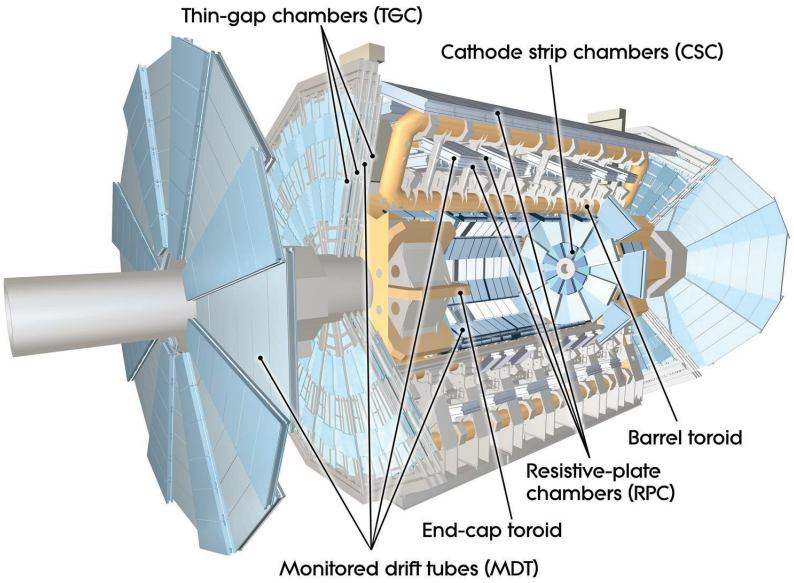

Figure 2–7: A cut-away view of the ATLAS Muon Spectrometer System [32].

able to pass through matter with minimal energy loss. It is instrumented with high-precision tracking chambers and a standalone trigger system. The measurement of muon trajectories is achieved using drift tubes in the barrel region and cathode strip chambers at large η, providing a total η coverage of up to $|\eta| < 2.7$. The independent trigger system uses resistive plate chambers in the barrel and thin gap chambers in the end-cap regions covering $|\eta| < 2.4$.

2.2.5 Trigger and Data Acquisition System

The trigger and data acquisition system [7] is designed to reduce the event data rate from ~ 40 MHz (the bunch crossing rate) to about 200 Hz. Only events where there is a direct collision or hard scattering are interesting from a physics standpoint. Therefore decisions are made at three levels to filter down the events while keeping

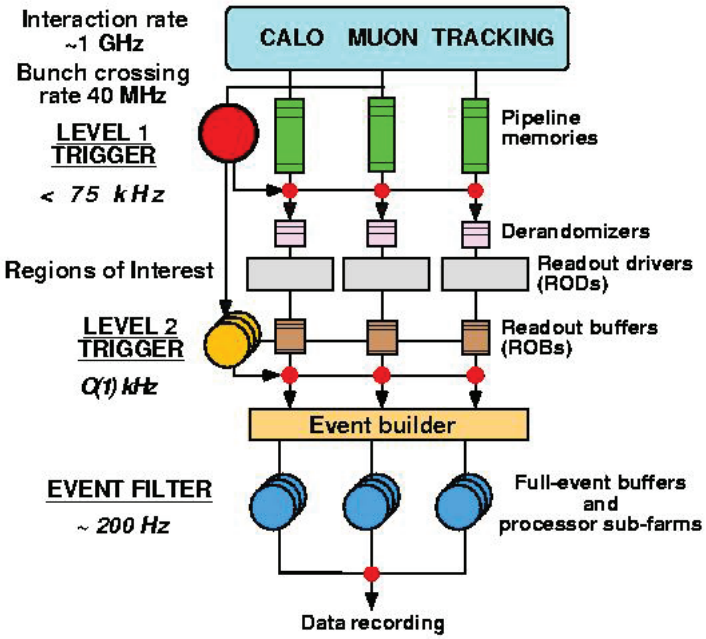

Figure 2–8: A flow chart of the ATLAS trigger and data acquisition system [33].

the hard scattering events. These three levels are shown in Figure 2–8 and are referred to as the level-1 trigger, level-2 trigger and event filter.

The Level-1 trigger is implemented using custom made electronics specific to ATLAS. Using information from the muon trigger and the calorimeter system, the level-1 trigger identifies interesting events and regions-of-interest[6] (ROIs) in the detector. The data rate is reduced from ~ 40 MHz to about 75 kHz with a decision time of about 2.5 μs. The region-of-interest information from level-1 is used to seed the reconstruction algorithms at the level-2 trigger.

[6] Areas in $\eta - \phi$ space where there was significant energy deposited.

The level-2 trigger then has access to event data fragments from different sub-detector systems in order to analyze the event further. However, it usually only uses data within specific η-ϕ regions given by the level-1 trigger to minimize the processing time. This further reduces the data rate to below 3.5 kHz with an average processing time of approximately 40 ms.

Events which pass the level-2 trigger are passed to the event filter where more elaborate selection algorithms are used to process the events. The event filter takes about one second to process one event and reduces the event rate to about 200 Hz. Once an event has passed the event filter it is copied to permanent storage. Together, the level-2 and event filter are called the high-level trigger. They are implemented using commercially available computers and networking hardware.

At the ends of the inner detector approximately 3.6 m from the nominal centre of the detector or interaction point lies the minimum-bias trigger scintillator (MBTS) detectors [34]. These detectors are important because they provide a trigger for low p_T particles for studies that may involve minimum particle p_T thresholds of only 100 MeV [35]. The MBTS detectors consist of 2 rings of 2 cm thick polystyrene scintillators segmented into 8 sections in ϕ and covering $2.09< |\eta| <2.82$ and $2.82< |\eta| <3.84$. Wavelength shifting fibres embedded within the scintillators read out each section.

2.3 ATLAS Forward Calorimeters

The ATLAS forward calorimeters [4] are located at both ends of the detector between the hadronic end-cap calorimeters and the beamline. Large amounts of low p_T collisions are produced in the high luminosity environment at the LHC which

bombard the detector with background particles. This means that persistent levels of ionization within the electrode gaps will be maintained for components such as the end-cap liquid argon calorimeters and the forward calorimeters (FCals) at each bunch crossing. These low p_T particles have the highest multiplicity in the forward regions, making it difficult when designing the FCals.

The search for beyond Standard Model physics relies heavily on missing transverse energy (E_T^{miss}). The FCal plays an important role in this by significantly increasing the hermiticity of the detector covering the η range $3.2 < \eta < 4.9$. There are also physics processes such as Vector Boson fusion [36], which produce jets in the forward regions that need to be properly identified. Processes of this nature impose the performance requirements on the FCal design. This means that the FCAL,

- must be radiation hard ensuring long-term stability at peak luminosities.
- should increase hermiticity to improve the accuracy of the E_T^{miss} measurement, making physics signals more prominent.
- should have efficient and precise energy measurements for jets.
- should have a fast response on the order of 25 ns, to minimize the effects of pileup[7] .

[7] Pileup refers to lingering signals in the calorimeter from a previous bunch crossing as well as multiple hard scattering collisions occurring in one bunch crossing. This is a significant effect in the 2012 data.

2.3.1 Design

The two forward calorimeter systems (one at each side of the interaction point) are each divided into three instrumented modules, FCal1, FCal2 and FCal3 and a fourth un-instrumented brass module (plug), as shown in Figures 2–9 and 2–10. They are arranged longitudinally along the beamline with the FCal1 module 4.7 m from the interaction point followed by the FCal2, FCal3 and plug modules. The FCal1 module provides the electromagnetic calorimetry and its passive material is made of copper. The FCal2 and FCal3 modules use tungsten instead of copper and provide the hadronic calorimetry. Tungsten was used to ensure better containment of hadronic particle jets within the limited space of the forward calorimeters. Lastly, the brass plug prevents any highly energetic secondary particles from punching through and interfering with the muon spectrometer.

The geometry of the FCal modules, as shown by Figure 2–11, was designed to deal with the high fluxes of low p_T particles brought on by the LHC. High particle fluxes can cause ion buildup within the liquid argon gaps. This can be overcome by reducing the gap sizes to approximately 2 mm which is 1/8 of the normal gap size. To achieve such small gaps the conventional design of parallel plates perpendicular to the beam line was dismissed and the current novel design was implemented, illustrated in Figure 2–11. Each module is composed of a matrix of longitudinal electrodes parallel to the beam line. The electrodes consist of a cylindrical copper cathode tube around an absorber anode rod, separated by a liquid argon gap. The liquid argon gaps

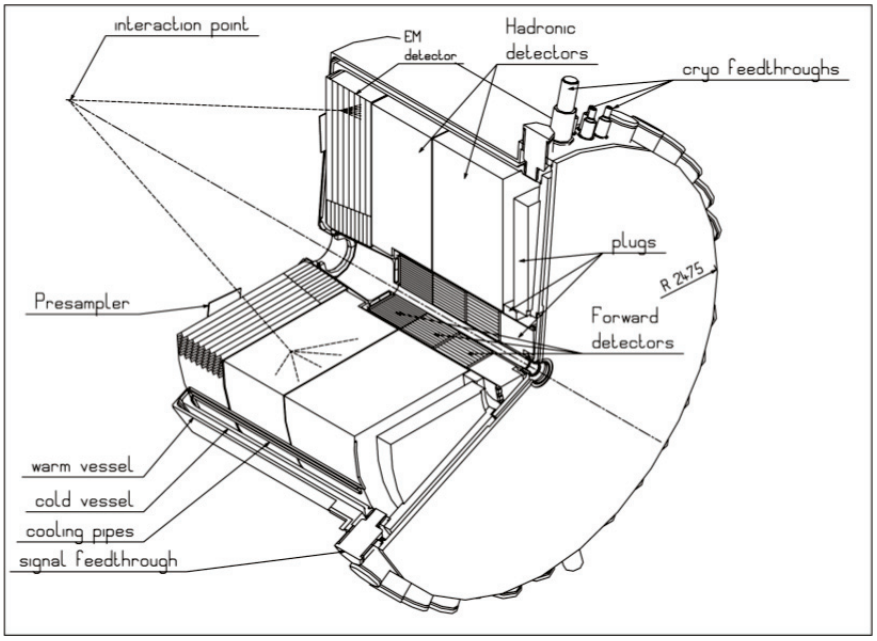

Figure 2–9: A cut away view of one complete end-cap and forward calorimeter module within a single cryostat [4].

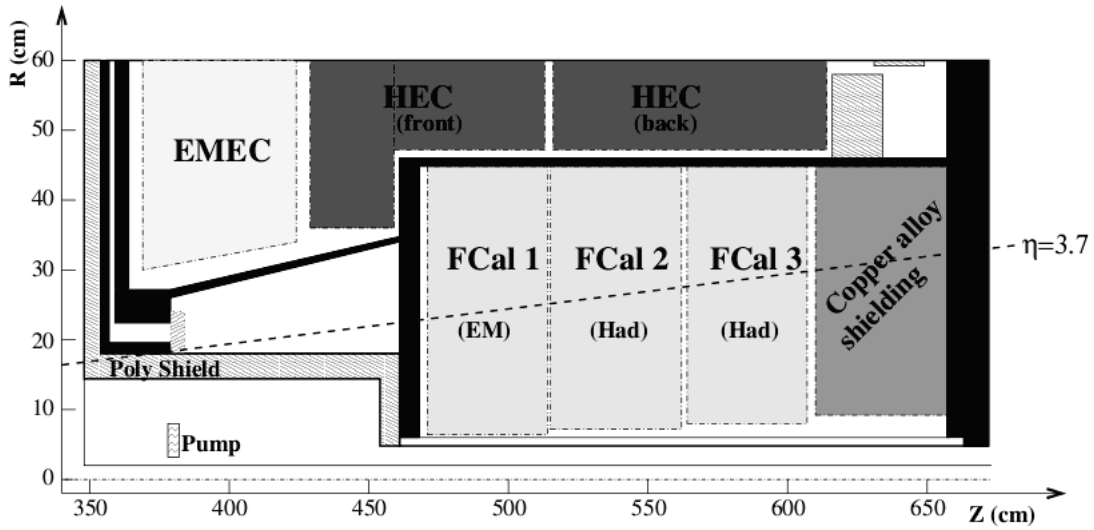

Figure 2–10: A longitudinal cross-section of the forward calorimeter modules [4].

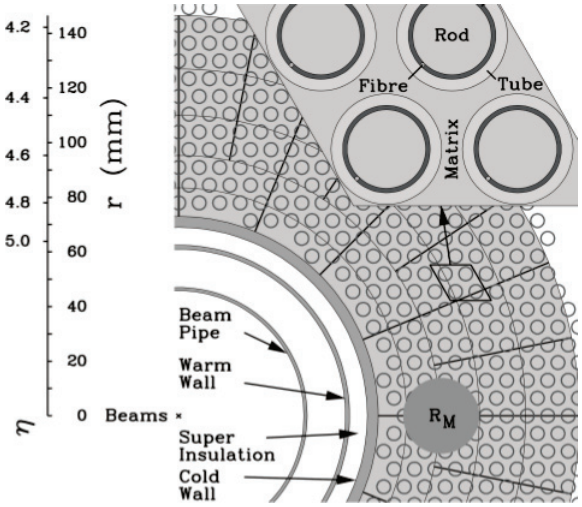

Figure 2–11: The transverse cross-section of the FCal1 module showing the hexagonal geometry of the electrode matrix [4].

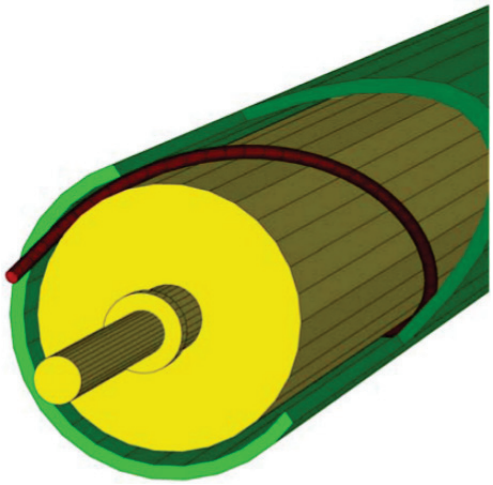

Figure 2–12: An enhanced view of the electrode design in the FCal modules [4].

are held at a fixed distance by a PEEK[8] fibre which is wound in a helical fashion around the absorber rod as shown in Figure 2–12. The electrodes are arranged in a hexagonal geometry with an electrode-electrode distance of 7.5 mm, 8.18 mm and 9 mm in FCal1, FCal2 and FCal3 modules, respectively. Electrodes are clustered into groups of 4, 6 and 9 for FCal1, FCal2 and FCal3 respectively. The signal from four groups are summed into a single read-out channel. The signal is then sent via the cryostat feed-through lines to the front-end buffers located at the back of the hadronic end-cap calorimeters.

[8] PolyEther-Ether-Ketone is a heat and radiation resilient thermo-plastic described in great detail in Reference [37].

The performance of the final FCal design was tested using electron and pion beams ranging in momenta from 10 GeV/c to 200 GeV/c. The parametrized energy resolution for the electron and pion beams were found to be $28.5\%/\sqrt{E}\oplus$ 3.5% and $94\%/\sqrt{E}\oplus$ 7.5%, respectively [4]. The expected energy resolution for the forward calorimeters is $100\%/\sqrt{E}\oplus$ 3.5% [7].

CHAPTER 3
Jets

One of the main reconstructed objects used at ATLAS in physics and performance analyses are jets. Two important quantities in data analyses are the jet energy scale and the jet energy resolution. The jet energy scale relates the measured energy of a jet to the energy of the parton which created it. The jet energy resolution represents the possible variance in the measured jet energy value. A brief description of how jets are constructed, found and calibrated will be discussed in this chapter.

3.1 Jet Reconstruction Inputs

The calorimeter system is the primary system used in the detection of jets and is segmented into approximately 270 000 calorimeter cells of varying sizes. To minimize the time it takes to reconstruct all of the jets in an event, larger calorimeter objects are created from the calorimeter cells. The *calorimeter topological cell clusters* or topoclusters are one of these larger calorimeter objects that are used by jet reconstruction algorithms [18].

Topoclusters are three-dimensional objects or "blobs of energy deposits" which have a well-defined position and energy. They are constructed by first identifying *seed* cells which are calorimeter cells with signal-to-noise ratio above a threshold t_{seed}. The signal-to-noise ratio is defined by,

$$\Gamma = E_{cell}/\sigma_{noise,cell} \tag{3.1}$$

where E_{cell} is the measured energy of the cell and $\sigma_{noise,cell}$ is the expected root-mean-square of the electronics noise for the current gain and calorimeter conditions for that cell. The seed cells are then listed in descending values of signal-to-noise ratio. For each seed cell, the neighbouring cells in all three dimensions are then tested to see if they pass a certain signal-to-noise threshold, $t_{neighbour}$. If the neighbouring cells pass the threshold they are combined with the seed cell to form a cluster of cells. The last step in the clustering algorithm is to add the cells around the neighbour cells to the cluster provided they pass the signal-to-noise threshold, t_{cell} [38]. Once these initial clusters are formed they are scanned for local signal maxima. If more than one local signal maxima are found within a cluster, then an algorithm is applied that splits the cluster between the maxima that are found [18].

The energy of topoclusters is defined as the sum of the energy of all the cells contained in the cluster. The energy of topoclusters is evaluated at the electromatgnetic energy scale. Jet reconstruction algorithms (next section) can be applied to these topoclusters to form jets with energy evaluated at the electromagnetic scale. Topoclusters can also be calibrated before being used to form jets. This calibration brings their energy from an electromagnetic scale to a local hadronic energy scale. By using information such as their shape and location, topoclusters are classified as being produced by electromagnetic particles (γ, $e^{\pm}$), hadronic particles or just noise signatures. The topoclusters are then corrected for inactive or dead material in or around them and out-of-cluster radiation to compensate for any cells that may have been missed in their formation. These calibration corrections are derived through studies of simulated data [39].

3.2 Reconstruction Algorithms

Jet reconstruction algorithms have evolved over the years to more accurately find and reconstruct showers of particles within calorimeters. There are a few experimental and theoretical attributes that are required for an ideal algorithm [40].

The theoretical attributes include:

- *Infrared safety*: Soft radiation stemming from processes occurring away from the hard scattered parton should not affect the number of reconstructed jets.
- *Collinear safety*: Reconstruction of a jet should not be affected by whether a certain amount of transverse momentum is caused by one or two collinear particles.
- *Invariance under boosts*: The algorithm should reconstruct the same jets despite any kinematic boosts in the longitudinal direction.
- *Boundary stability*: The kinematic variables describing the jets should have kinematic boundaries that are insensitive to the details of the final state[1] . This criteria is important in order to perform soft gluon summations.
- *Order independence*: The same jets should be found at the parton, particle or detector levels independently.
- *Straightforward Implementation*: The algorithm should not be complicated to implement in perturbative calculations.

[1] An example of this is the kinematic variable E_T. This variable is sensitive to the number of particles present as well as their relative angles. The maximum value of E_T for a collinear particle or massless jet is $\sqrt{s}/2$ where $\sqrt{s}$ is the centre of mass energy of the collision. For massive jets the maximum value for E_T can be larger.

The experimental attributes include:

- *Detector independence*: The algorithm should not depend on detector attributes such as segmentation, resolution or energy response.
- *Minimization of resolution effects*: The algorithm should minimize the degradation of the energy resolution of the jets found.
- *Stability with luminosity*: At high luminosities, the amount of hard scatterings should not strongly affect the jet finding or their energy and angular resolutions.
- *Efficient use of computer resources*: Minimum computer processing time should be used when identifying jets.
- *Maximal reconstruction efficiency*: All interesting jets stemming from hard scattering should be efficiently identified.
- *Ease of calibration*: The algorithm should not interfere with the calibration of the final kinematic properties of the jets.
- *Ease of use*: The algorithm should be easy to implement with experimental detectors and data.
- *Fully specified*: The algorithm must be complete in specifying all details for clustering, energy and angle definitions and combining jets together or splitting them apart.

Jet finding algorithms are designed with the above attributes in mind. The two classes of clustering algorithms that have been developed over the previous years are "cone-type" and "sequential recombination" algorithms. None of the "cone-type" algorithms are used in this analysis so they will not be discussed any further. If desired, information on them can be found in Reference [40]. The k_T and anti-k_T

algorithms are the most commonly used sequential recombination algorithms and are discussed in the next two sections.

The k_T Algorithm

The k_T algorithm starts with a list of pre-clusters, which for this analysis are topoclusters and an empty list of jets. For pre-cluster i and every other pre-cluster j, the parameters d_{ij} and d_i are calculated using Equations 3.2 and 3.3 respectively. The parameter d_i is just the transverse momentum of pre-cluster i and the variable D is a parameter of the jet algorithm which allows for some input as to the size of the reconstructed jets.

$$d_{ij} = min\left(p_{Ti}^2, p_{Tj}^2\right) \frac{(\eta_i - \eta_j)^2 + (\phi_i - \phi_j)^2}{D^2} \tag{3.2}$$

$$d_i = \left(p_{Ti}^2\right) \tag{3.3}$$

The parameters d_{ij} and d_i are then compared. If $d_{ij} < d_i$ then the four-momentum vectors of pre-clusters i and j are merged, defining a new "pre-cluster" k. Pre-clusters i and j are then removed from the pre-cluster list and replaced with k. However, if $d_i < d_{ij}$ then i is removed from the pre-cluster list and added to the list of jets. The last pre-cluster in the pre-cluster list is labelled as a jet and added to the list of jets. These steps are repeated until the pre-cluster list is empty, leaving a list of reconstructed jets [40]. Every cluster is either merged into a jet or defined itself as a jet with no overlap. Therefore this algorithm is infrared safe because the introduction of soft radiation to the event won't effect the number of jets found. This algorithm is also collinear safe because it has no dependency on seeds or where it starts clustering

topoclusters to form jets. The default settings in ATLAS are $D = 0.4$ for narrow and $D = 0.6$ for wide jets.

The Anti-k_T Algorithm

The anti-k_T algorithm works in precisely the same way as the k_T algorithm with one change in the definition of the parameters. The parameters d_{ij} and d_i are defined as:

$$d_{ij} = min\left(\frac{1}{p_{Ti}^2}, \frac{1}{p_{Tj}^2}\right)\frac{(\eta_i - \eta_j)^2 + (\phi_i - \phi_j)^2}{D^2} \tag{3.4}$$

$$d_i = \left(\frac{1}{p_{Ti}^2}\right) \tag{3.5}$$

The slight difference in the parameters d_{ij} and d_i causes very different methods of clustering. By definition, the k_T algorithm clusters soft particles together first, clustering the highest p_T particles last. The anti-k_T algorithm, however identifies the highest p_T particles and clusters the lower p_T particles to them. This leads to faster processing times than the k_T algorithm. Like the k_T algorithm the anti-k_T algorithm is also infrared safe.

3.3 Jet Energy Scale

A requirement of good calorimetry is that there is a uniform *response* to jets in every region of the detector. A uniform jet response means that the measured energy of a jet is independent of the jets' location within the detection. Unfortunately there are inhomogeneities within the detector which prevent certain regions from reconstructing events as efficiently as other regions. This leads to a non-uniform response throughout the detector. It is therefore essential that a calibration is applied in order to restore the uniformity of the jet energy response as much as possible.

The jet energy scale is another correction applied to a reconstructed jet that translates the jet's energy from the measured electromagnetic energy scale to the hadronic energy scale. Contributions to the jet energy scale come from detector and physical effects which cause inaccurate jet energy and/or momentum measurements. Detector effects include non-instrumented regions of the detector such as cracks between sub-systems and dead material, as well as the finite energy resolution and cell granularity of the calorimeters. Physical effects are primarily the consequences of the limitations of the jet finding algorithms. Particles created during the fragmentation of the original parton may be merged into neighbouring jets or identified as a single soft jet (out-of-cone radiation) causing the reconstructed jet to have a lower energy than it should. The inclusion of out-of-cone radiation or other particles not from the original parton may also be merged into the jet causing an erroneous jet energy. These other particles can come from underlying events[2] and/or pileup.

Currently a jet-by-jet calibration scheme is applied to jets based on their energy and pseudorapidity at the electromagnetic scale. This scheme is carried out in three steps;

1. Correction constants are derived from *in situ* measurements and used to subtract the average additional energy due to pileup from the energy measured in the calorimeters.

[2] Underlying events are any soft-collisions occurring with the hard scattering collision simultaneously.

2. Jet position corrections are applied such that the origin of each jet is taken as the primary vertex and not the geometrical centre of the the ATLAS detector.
3. Corrections are derived from the comparison of reconstructed and truth jet properties in simulated data and then applied to the reconstructed jet energy and position.

For this calibration, correction factors are obtained for different $|\eta|$ regions or bins ranging from $0 < |\eta| < 4.4$ for jets with p_T at the electromagnetic scale ($p_T^{EMscale}$) greater than 10 GeV/c. The correction factors found for $p_T^{EMscale} = 10$ GeV/c are applied to all of the jets with $p_T^{EMscale} < 10$ GeV/c for their respective $|\eta|$ regions [39]. When this calibration scheme is used the jet energy scale is restored to within 2% for the full kinematic (energy and momentum) range [41]. This means that the response of the detector within $0 < |\eta| < 4.4$ is within 2% of unity when this calibration is used. It is also important to validate and/or correct these corrections with data collected early using *in situ* techniques such as QCD di-jet balancing [42] and transverse momentum balancing using γ/Z+jets events [43, 17].

3.4 Jet Energy Resolution

The jet energy resolution is another important measurement. It represents the precision to which one can measure the energy of a jet. For example, if a beam of particles at a known energy hits a calorimeter the energy measured by the calorimeter would not be a δ-function at the correct energy. Instead the calorimeter would measure a Gaussian-like distribution around a mean approximately equal to the correct energy. This implies that the absolute energy resolution can be characterized by the width of the distribution produced by the calorimeter energy measurements.

There are three contributions to the smearing of the measured jet energy. They are stochastic fluctuations (S), noise fluctuations (N) and a constant term (C). Stochastic fluctuations are caused by event-to-event differences in the properties of the jets such as particle composition or the ionization processes it has undergone. These fluctuations are modelled by Poisson statistics. Electronic noise within the ATLAS calorimeters can cause inconsistencies in the jet energy measurements and therefore contribute to the noise fluctuations. The constant term is caused by detector effects such as non-instrumented regions, cracks between sub-systems and the non-compensation of the detectors. The jet energy resolution can be parametrized in terms of these three contributions:

$$\frac{\sigma_{p_T}}{p_T} = \frac{S}{\sqrt{p_T}} \oplus \frac{N}{p_T} \oplus C \tag{3.6}$$

where p_T, σ_{p_T} and N are in units of GeV/c, S is in units of $\sqrt{\text{GeV/c}}$ and C is unit-less. The analysis techniques used to study the jet energy resolution using simulated data cannot be used with real data since there is no truth information. Therefore *in situ* techniques are used with experimental data to determine the jet energy resolution as well as the jet energy scale.

This thesis uses narrow jets ($D = 0.4$) reconstructed with topoclusters using the anti-k_T algorithm which are calibrated with the current ATLAS calibration scheme. Narrow jets were chosen in order to ensure that the jets found in the FCALs were fully contained within the detector. Using these reconstructed jets, the jet energy scale and resolution of the ATLAS forward calorimeters are determined by implementing the di-jet balance method described in the next chapter.

CHAPTER 4
Methodology

This chapter will outline the di-jet balance method used to determine the jet energy scale and resolution of the ATLAS forward calorimeters. A brief description of the data used will start the chapter followed by an outline of the di-jet balance method and event selection. An outline of the procedure to determine the jet energy scale and resolution will complete the chapter.

4.1 ATLAS 2010 Data

This analysis uses data recorded by the ATLAS detector from March to the end of December 2010, corresponding to an integrated luminosity of approximately $35\,pb^{-1}$. Before the data were used, a detector status filter was applied to ensure that all of the detector systems were at nominal working conditions when the data was collected. Approximately 70% of the data passed this filter.

4.2 The Di-jet Balance Method

The di-jet balance method employs the principle of transverse momentum conservation. When there are two final state partons after a hard scattering event, the vector sum of the total transverse momentum of the calorimeter jets should equal zero. In reality though, not all of the parton's energy will be represented by the resulting calorimeter jets because of the detector and physics effects mentioned in Section 3.3. The difference between the two jet momenta can be used to quantify information about the detector such as the jet energy scale and resolution.

The di-jet balance method searches for di-jet events where one jet is in a reference region (the *Tag* jet) and the other jet is in a region of the detector that is to be investigated (the *Probe* jet). The reference region is chosen to be a region of the detector that is well calibrated and understood and the probe region is where a calibration should be done. For every di-jet event found, an asymmetry variable is calculated using the Tag and Probe jets. The asymmetry variable is defined as;

$$A = \frac{\left(p_T^{Tag} - p_T^{Probe}\right)}{p_T^{Tag}} = 1 - \frac{p_T^{Probe}}{p_T^{Tag}} \tag{4.1}$$

and is asymmetric by construction with a maximum at 1 and a minimum at $-\infty$. An alternative definition that is commonly used in ATLAS analyses is,

$$A_{p_T^{Ave}} = \frac{\left(p_T^{Tag} - p_T^{Probe}\right)}{p_T^{Ave}} \tag{4.2}$$

where p_T^{Ave} is the average p_T between the tag and probe jets given by,

$$p_T^{Ave} = \frac{p_T^{Tag} + p_T^{Probe}}{2}. \tag{4.3}$$

This definition is more symmetric than Equation 4.1 with a minimum at -2 and a maximum at 2, however determining the relationship between the Tag and Probe jets is more complicated. Asymmetry variables that are calculated with Equation 4.1 and 4.2 are binned with respect to the p_T^{Tag} and p_T^{Ave} of the event, respectively.

Asymmetries that arise in the distributions produced with Equations 4.1 and 4.2 can lead to biases when determining the relationship between the Tag and Probe jets. Besides the algebraic nature of each definition, the event-by-event fluctuations or variances of the Tag and Probe jet p_T can contribute to the asymmetry of the

distributions. In order to investigate this effect the p_T of the Tag and Probe jets was generated on an event-by-event basis based on two random Gaussian distributions (one for the Tag jet p_T and one for the Probe jet p_T) [17]. The width or standard deviations (σ_{p_T}) of the Gaussian distributions were left as parameters to vary and the means were fixed at a value of 30 GeV/c. For each generated value of p_T^{Tag} and p_T^{Probe}, Equations 4.1 and 4.2 were calculated and binned producing a distribution for each definition. The cases where $\sigma_{p_T^{Tag}} < \sigma_{p_T^{Probe}}$, $\sigma_{p_T^{Tag}} > \sigma_{p_T^{Probe}}$ and $\sigma_{p_T^{Tag}} = \sigma_{p_T^{Probe}}$ were investigated. The values of σ_{p_T} = 6 GeV/c and 10 GeV/c were chosen to investigate each case because they are the energy resolution estimates for a jet with p_T = 30 GeV/c found in the barrel and forward calorimeter regions, respectively [44].

Figure 4–1a illustrates the asymmetry distributions for Equations 4.1 and 4.2 for the case where $\sigma_{p_T^{Tag}}$ = 6 GeV/c and $\sigma_{p_T^{Probe}}$ = 10 GeV/c. The distribution given by Equation 4.2 is slightly more symmetric than the distribution for Equation 4.1 however it has a peak location further away from $\langle A \rangle = 0$. Since both the p_T^{Tag} and p_T^{Probe} are randomly generated by two Gaussian distributions with the same mean, a peak at 0 is the most desirable and accurate asymmetry value.

Figure 4–1b depicts the opposite case where $\sigma_{p_T^{Tag}}$ = 10 GeV/c and $\sigma_{p_T^{Probe}}$ = 6 GeV/c. In this case distribution given by Equation 4.2 has a peak location closer to 0 however both distributions are quite asymmetric.

Figure 4–2 shows the final case where $\sigma_{p_T^{Tag}} = \sigma_{p_T^{Probe}}$ = 6 GeV/c. Here the distribution for Equation 4.2 is significantly more symmetric than that of Equation 4.1 and has a peak location that is closer to 0. The incorporation of both the Tag and

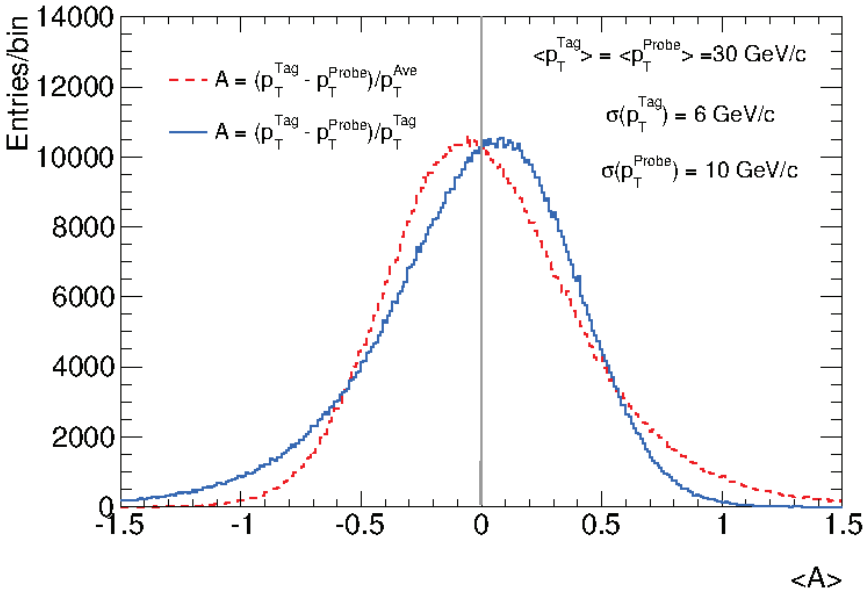

(a) $\sigma(p_T^{Tag}) < \sigma(p_T^{Probe})$

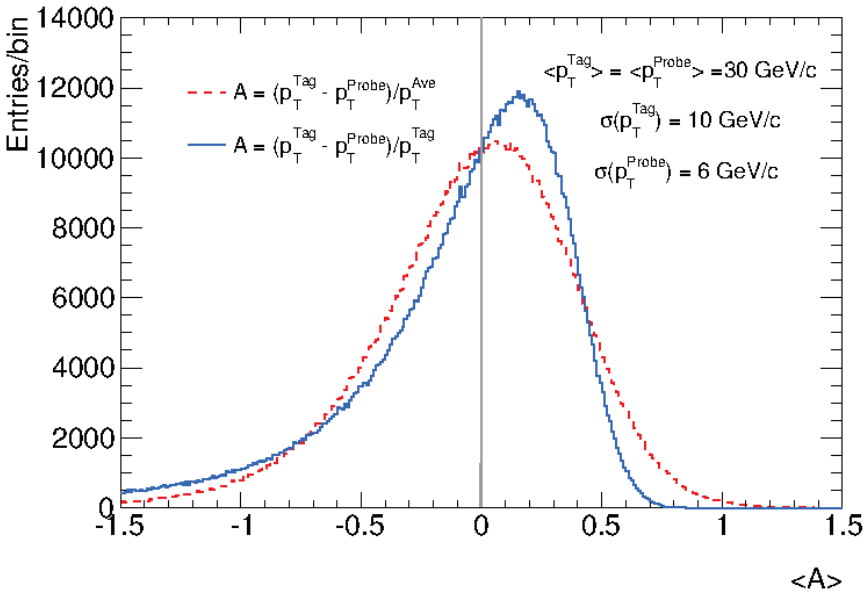

(b) $\sigma(p_T^{Tag}) > \sigma(p_T^{Probe})$

Figure 4–1: Comparison of the asymmetry distributions for the definitions given by Equations 4.1 and 4.2 for the cases where the variance of the Tag jet is (*a*) less than that of the Probe jet and (*b*) greater than that of the Probe jet.

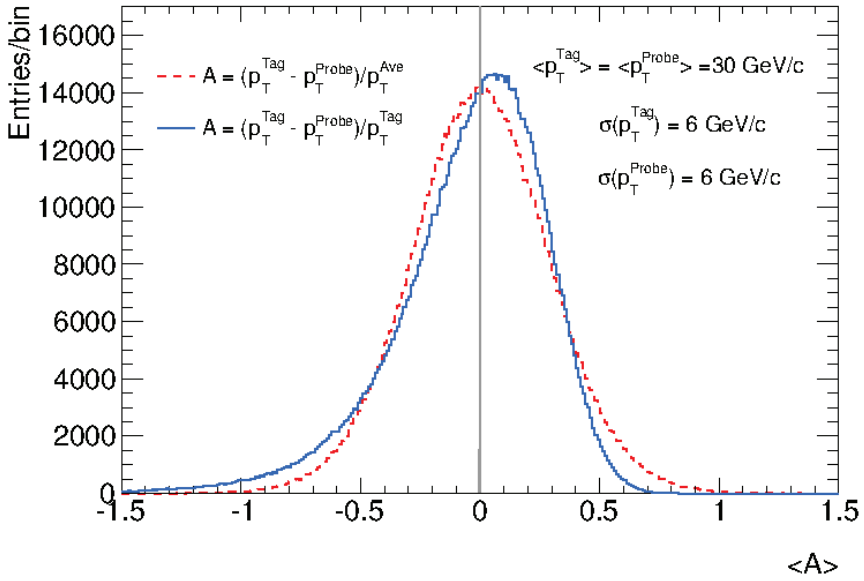

Figure 4–2: Comparison of the asymmetry distributions for the definitions given by Equations 4.1 and 4.2 for the case where the variance of the Tag jet is equal to the Probe jet variance ($\sigma\left(p_T^{Tag}\right) = \sigma\left(p_T^{Probe}\right)$).

Probe jet transverse momenta in the normalization factor or denominator of equation 4.2 introduces a bias when determining the relationship between the Tag and Probe jets. This makes it difficult to estimate the jet energy resolution using the di-jet balancing technique presented in this thesis. The jet energy resolution is expected to be worse in the forward calorimeters than in the barrel region based on the expected energy resolutions for each calorimeter discussed in Sections 2.2.3 and 2.3. The trends shown in Figures 4–1 and 4–2 imply that the asymmetry definition given by Equation 4.1 is best suited when probing a region that has a worse resolution than the reference region or specifically when $\sigma_{p_T^{Tag}} < \sigma_{p_T^{Probe}}$. Therefore Equation 4.1 will be used for the remainder of this thesis unless otherwise stated.

4.2.1 Di-jet Event Selection

The basic event topology enforced in this analysis requires that there are at least two jets that are back-to-back in the transverse plane, with one of the two highest p_T jets in the reference region of the detector and the other in the probe region. The following selection cuts were applied to the data in order to obtain an enriched sample of events with that topology.

Trigger Strategy

The ATLAS jet triggers were used in order to maximize the likelihood that only hard-scattering events were selected for this analysis. Table 4–1 outlines the trigger strategy used. For every bin in p_T^{Tag} the highest threshold single jet trigger that had a >99% efficiency identifying events of interest was chosen. Figure 4–3 depicts the

p_T^{Tag} **Bins [GeV/c]**	**Data-taking periods**	
	A-F	G-I
20-40	`L1_MBTS_1`	`EF_mbMbts_1_eff`
40-50	`L1_J5`	`None`
50-60	`L1_J10`	`EF_j30_jetNoEF`
60-70	`L1_J15`	`EF_j35_jetNoEF`
70-80	`L1_J15`	`EF_j35_jetNoEF`
80-110	`L1_J15`	`EF_j35_jetNoEF`
110-160	`L1_J30`	`EF_j50_jetNoEF`

Table 4–1: Table listing the trigger items used for the analysis for each data-taking period.The trigger items for periods A-F are evaluated by the level-1 selection criteria only hence starting with "L1". For periods G-I, the trigger items are evaluated with level-2 and the event filter selection criteria however only level-2 makes event selections. The event filter algorithm was running but no decisions were made hence "EF_jX_jetNoEF". The trigger items with "J" or "j" are jet triggers which look for events with at least one jet with $\geq$ X GeV of energy at the electromagnetic scale, where "X" is the number following the J or j. The "MBTS" and "mbMbts" triggers are minimum-bias triggers based on the MBTS detectors discussed in Section 2.2.5.

efficiency curves for the jet triggers which motivated the trigger strategy in Table 4–1. The triggers used are at $\sim 99\%$ efficiency for the entire p_T^{Tag} range of that bin to prevent any possible trigger biases.

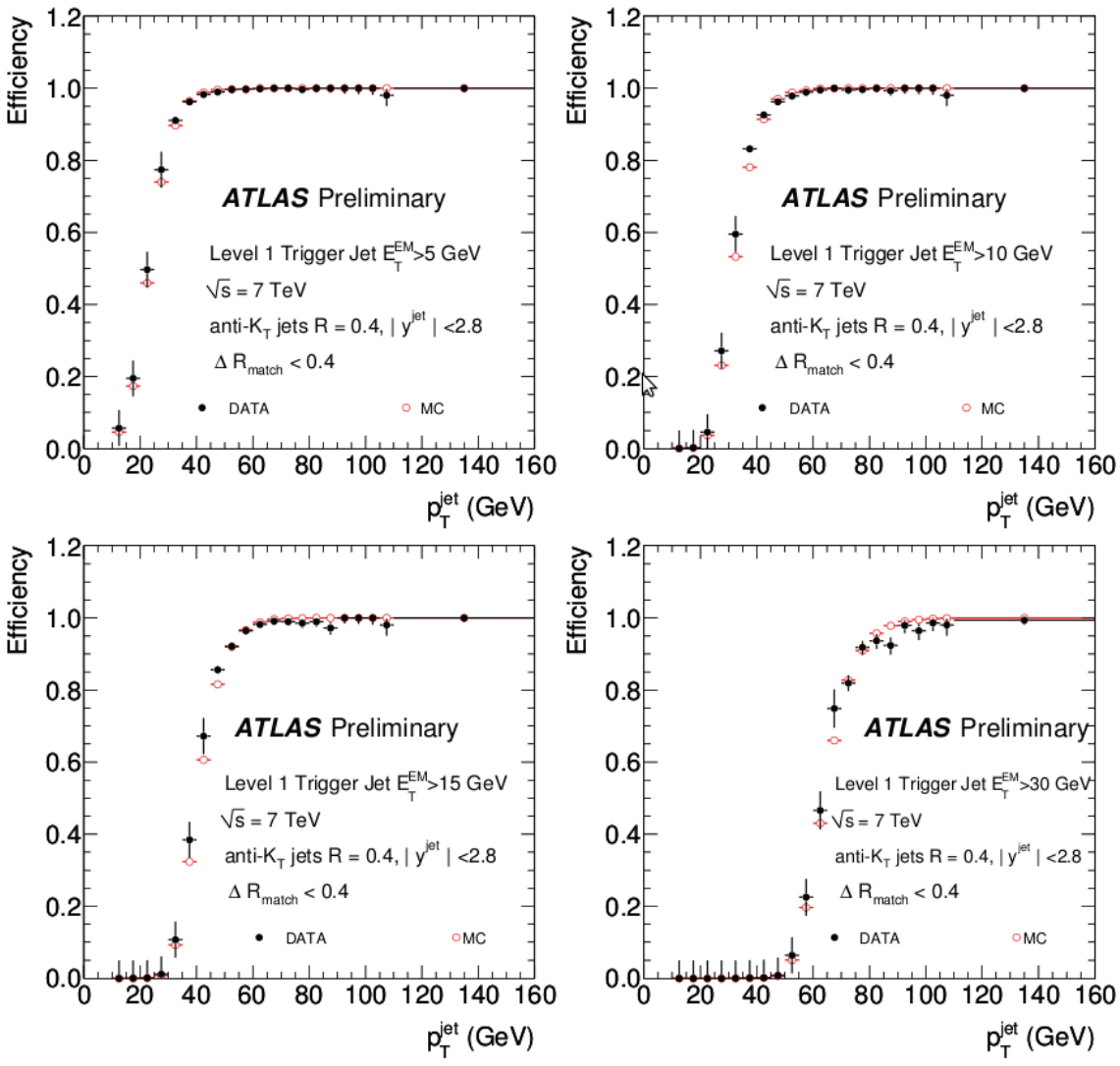

Figure 4–3: Trigger efficiency curves for the L1_J5 (top left), L1_J10 (top right), L1_J15 (bottom left) and L1_J30 (bottom right) level-1 jet triggers [45]. The jet p_T (x-axis) for each figure is measured at the EM+JES scale.

The lowest energy jet trigger (L1_J5) has a threshold of 5 GeV[1] , however only becomes 99% efficient at approximately 40 GeV at the EM+JES scale [46]. This is due to two different effects. First, there is a difference in energy scales between the level-1 trigger energy threshold (EM scale) and the offline jet calibrated energy scale (EM+JES scale) as described in Section 3.3. The size of the jet energy scale correction factors depend on the jet energy and position, and typically vary from 1.2 to 1.8. Secondly, in order to maintain fast event-by-event decision times, the level-1 jet trigger scans the calorimeter to find energy maxima within regions of maximum size 0.8×0.8 in $\Delta\eta \times \Delta\phi$. This causes poor level-1 energy resolution and the large discrepancy between threshold and efficiency energies seen in Figure 4–3.

In order to minimize any biases caused by the trigger selection, the minimum bias triggers are used to populate the low p_T bin. The minimum bias triggers are fully efficient for a p_T range well below what is used in this analysis and have negligible trigger biases [47].

The level-1 triggers were used for periods A to F because the high-level trigger selection was not rejecting events during that time. At the beginning of period G the high-level trigger was turned on however only the level-2 trigger began rejecting events. Events were going through the event filter algorithm but were not being selected or rejected. Therefore events in Periods G-I were selected based on event filter triggers using the level-2 trigger selection criteria. No fully efficient unprescaled

[1] Energy measured by the level-1 trigger at the electromagnetic scale.

single jet event filter trigger was found for the 40-50 GeV/c p_T bin so events from periods G-I were excluded from this bin.

Jet Selection

As mentioned in Section 3.3, jets used in this analysis were reconstructed using the anti-k_T algorithm applied to topological clusters with a distance parameter of D=0.4 and calibrated with the current ATLAS jet energy scale. The Tag and Probe jets were constrained to be the two highest p_T jets in the event. The Tag jet was required to be within a reference η region of $0.1 < |\eta| < 0.8$ which is located in the central barrel calorimeter. The region $|\eta| < 0.1$ was excluded due to small inhomogeneities in the detector at $\eta = 0$ where the two halves of the central barrel calorimeter are connected [39]. In order to investigate the forward calorimeter using the di-jet balance technique, the Probe jet was required to be within an η range of $3.6 < |\eta| < 4.4$. This ensured that the Probe jet was fully contained within the forward calorimeters. Jets located near the transition region between the forward and the hadronic end-cap calorimeters at $\eta = 3.2$ or near the beamline at $\eta = 5.0$ may not have been completely reconstructed which would have led to biases in the results.

The current ATLAS EM calibration is incomplete for jets with $p_T < 10$ GeV/c at the electromagnetic scale. Therefore all Tag and Probe jets were required to have a jet p_T at the electromagnetic scale greater than 10 GeV/c. This prevented any spurious mis-calibrated low p_T jets from biasing the results. The jets used were also required to be flagged as *good* jets. This requirement ensures that the reconstructed jet was formed by an actual particle and not mis-reconstructed from a sporadic noise

burst within the hadronic end-cap or electromagnetic calorimeters. More information about this requirement is outlined in more detail in Ref. [48].

Selection of Back-to-Back Jets

One of the main selection cuts for a di-jet event was to require that the Tag and Probe jets were back-to-back. This can be done by requiring that the difference in their ϕ coordinates, $|\Delta\phi| \approx \pi$ radians. This strict criterion greatly reduces the amount of di-jet events so a more practical requirement of $|\Delta\phi| > 2.6$ radians was implemented. Figure 4–4 shows how this cuts affects the amount of available di-jet events. A $|\Delta\phi|$ cut of 2.6 was chosen in order to maximize the available statistics. The distance parameter, D, of the jets used also motivated this choice. If the uncertainty

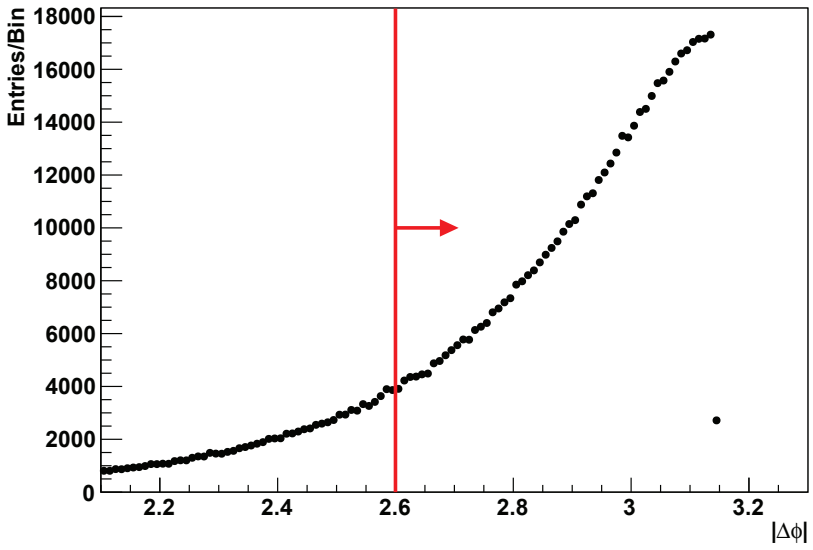

Figure 4–4: Diagram of the $|\Delta\phi|$ between the two highest p_T jets in $\geq$2-jet events. Jets are reconstructed using the anti-kt algorithm with D=0.4 and have passed the jet selection cuts discussed Section 4.2.1, with the exception of the $|\Delta\phi|$ cut.

in the measured direction of a jet is taken to be the distance parameter D, then adding the distance parameter of the Tag and Probe jets in quadrature will give an estimation of the uncertainty on the $|\Delta\phi|$ measurement. For jets with D=0.4, the error in $|\Delta\phi|$ is approximately 0.57 radians which implies that,

$$\begin{aligned} \Delta\phi &= \pi - 0.57 \text{ radians} \\ &\sim 2.6 \text{ radians.} \end{aligned} \tag{4.4}$$

Third Jet p_T Cut

Events with $\geq 3-$jets were used as long as the p_T of the 3^{rd} jet was not significant compared to the highest p_T jet or leading jet, in the event. The third, fourth and higher jets in the $\geq 3-$jet events are the result of gluons that have radiated off of the partons which created the two highest p_T jets in the event. The extra jets in the event can cause an imbalance between the p_T of the Tag and Probe jets. Therefore events with more than two jets were used if $F_3 < 15\%$, where F_3 is defined to be

$$F_3 = \frac{p_T^{3^{rd}Jet}}{p_T^{leading}}. \tag{4.5}$$

Restricting the third jet p_T in the event to be low ensures that any remaining jets are negligible for this calibration technique. Figure 4–5 shows the F_3 value and the corresponding $|\Delta\phi|$ value between the two highest p_T jets for 3–jet events. The horizontal and vertical black lines indicate the chosen nominal values for the F_3 and $|\Delta\phi|$ selection cuts respectively and the arrows show the direction of the events that are accepted. An F_3 value of 15% was chosen as the nominal value because it incorporates the peak of the F_3 spectrum which is also clustered around $|\Delta\phi| \sim 3.1$

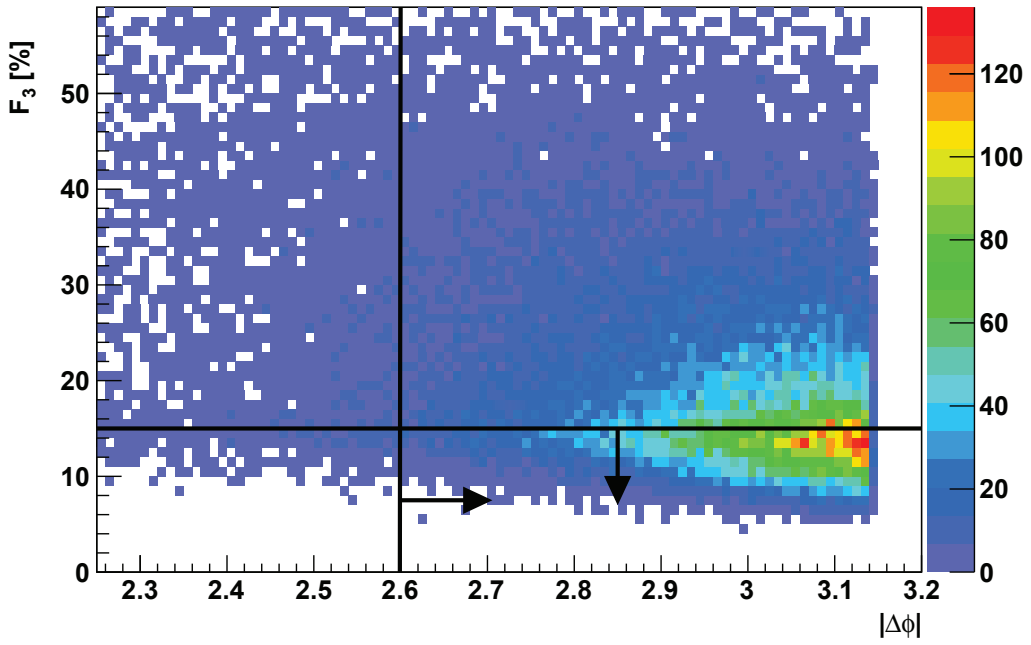

Figure 4–5: Diagram of the F_3 value and the corresponding $|\Delta\phi|$ value between the two highest p_T jets for 3−jet events. The horizontal and vertical lines represent the chosen nominal values for the F_3 and $|\Delta\phi|$ cuts respectively. The arrows show the accepted events after the cuts. The colour palette on the right shows the number of entries corresponding to each colour. Jets are reconstructed using the anti-kt algorithm with D=0.4 and have passed the jet selection cuts discussed Section 4.2.1, with the exception of the F_3 and $|\Delta\phi|$ cuts.

radians. Results obtained with events containing exactly 2−jet and 3 or more jets will be presented separately.

4.2.2 Fitting Procedure

The function chosen to fit the asymmetry distributions obtained by applying the selection cuts outlined in Section 4.2.1 was a single Gaussian. The single Gaussian

fit is defined by,

$$f(x) = p_0 e^{\frac{(x-p_1)^2}{2p^2}} \tag{4.6}$$

and consists of three parameters; the constant term (p_0), mean (p_1) and standard deviation (p_2). The single Gaussian fit was applied to the peak region of the asymmetry distributions. The peak region was defined to be within approximately 2 standard deviations away from the mean of the histogram. The mean and the root-mean-squared values of the histograms could have been used, however the asymmetric tails of the distributions would have biased the results. The fit was performed within a range chosen to optimize the χ^2 value and exclude the asymmetric tails, thus ensuring the most accurate representation of the peak location (mean) and width (standard deviation). If there were insufficient statistics or no reasonable fit was obtained, the corresponding p_T^{Tag} bin was not used for further analysis. Figure 4–6 illustrates this technique showing the asymmetry distribution for a particular p_T^{Tag} bin and the respective fit. Information about the relative jet energy scale and resolution ere determined from the fit parameters by following the methods discussed in the next two sections.

4.2.3 Determination of the Jet Energy Scale

The di-jet balance method compares a Tag jet in a well calibrated region of the detector with a Probe jet through the use of Equation 4.1. By re-arranging Equation 4.1 the relationship between the Tag and Probe jet p_T was determined to

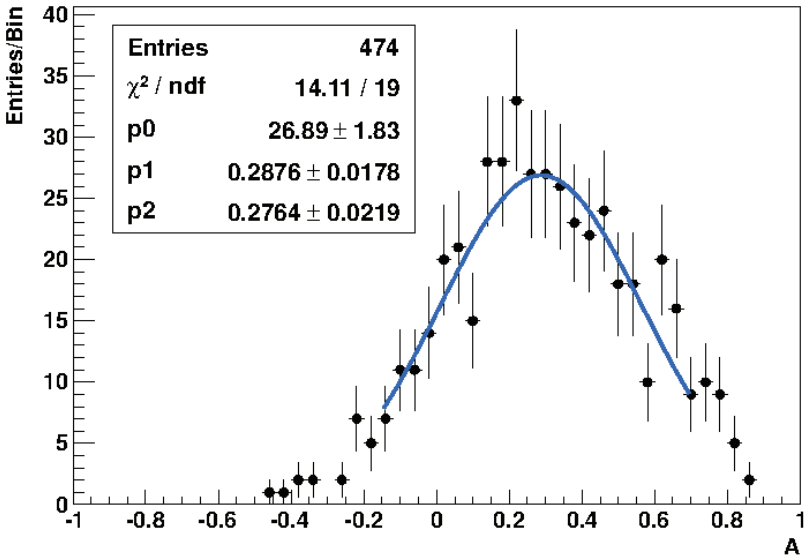

Figure 4–6: Diagram of the $60 < p_T^{Tag} < 70$ GeV/c bin for 2−jet events after applying the event selection described in Section 4.2.1. The vertical error bars are purely statistical.

be,

$$\begin{aligned} \frac{p_T^{Probe}}{p_T^{Tag}} &= 1 - A \\ \Rightarrow p_T^{Tag} &= \left(\frac{1}{1-A}\right) p_T^{Probe} \\ \Rightarrow p_T^{Tag} &= (k)\, p_T^{Probe} \end{aligned} \tag{4.7}$$

The correction factor k relates the energy scale of the Probe jet to that of the Tag jet. When the Tag and Probe jets are measured to have the same energy, k is equal to unity which implies that the event is balanced and $\langle A \rangle = 0$. If there is any deviation from unity the correction factor, k, can be used to correct the energy of the Probe jet to be that of the Tag jet.

This analysis was performed in 7 bins of p_T^{Tag} outlined in Table 4–1 and in one single bin of $|\eta|$. This binning was chosen such that there were sufficient statistics in most bins to provide meaningful Gaussian fits. The correction factors for each bin were calculated using,

$$\langle k \rangle = \frac{1}{(1 - \langle A \rangle)} \tag{4.8}$$

where $\langle A \rangle$ is the mean of asymmetry distribution fits. All statistical uncertainties related to quantities calculated with measured variables were computed using the general rules for error propagation [3]. The uncertainty on $\langle k \rangle$ was therefore determined to be,

$$\begin{aligned} \delta\langle k \rangle &= \sqrt{\left(\frac{\partial\langle k \rangle}{\partial\langle A \rangle}\right)^2 (\delta\langle A \rangle)^2} \\ &= \frac{\delta\langle A \rangle}{(1 - \langle A \rangle)^2} \end{aligned} \tag{4.9}$$

where $\langle A \rangle$ is the mean and $\delta\langle A \rangle$ is the uncertainty of the mean of the asymmetry distribution provided by a Gaussian fit.

4.2.4 Determination of the Jet Energy Resolution

The asymmetry distributions obtained using the di-jet balance method also provide information regarding the jet energy resolution of the Probe jet region. This

relationship can be found by using the variance of the asymmetry variable in Equation 4.1 defined by,

$$\begin{aligned}\sigma_A^2 &= \left(\frac{\partial A}{\partial p_T^{Tag}}\right)^2 \sigma^2_{p_T^{Tag}} + \left(\frac{\partial A}{\partial p_T^{Probe}}\right)^2 \sigma^2_{p_T^{Probe}} \\ &= \left(\frac{p_T^{Probe}}{\left(p_T^{Tag}\right)^2}\right)^2 \sigma^2_{p_T^{Tag}} + \left(\frac{-1}{p_T^{Tag}}\right)^2 \sigma^2_{p_T^{Probe}} \\ &= \left(\frac{p_T^{Probe}}{p_T^{Tag}}\right)^2 \left[\left(\frac{\sigma_{p_T^{Tag}}}{p_T^{Tag}}\right)^2 + \left(\frac{\sigma_{p_T^{Probe}}}{p_T^{Probe}}\right)^2\right]\end{aligned} \tag{4.10}$$

To simplify further, the p_T of the Tag and Probe jets are taken at their mean values of $\langle p_T^{Tag}\rangle$ and $\langle p_T^{Probe}\rangle$ for a di-jet event. Conservation of transverse momentum can then be applied such that $\langle p_T^{Tag}\rangle \approx \langle p_T^{Probe}\rangle = p_T$. By simplifying and rearranging Equation 4.10, the expression for the relative jet energy resolution of the Probe jet η can be given by,

$$\frac{\sigma_{p_T^{Probe}}}{p_T} = \left[\sigma_A^2 - \left(\frac{\sigma_{p_T^{Tag}}}{p_T}\right)^2\right]^{\frac{1}{2}}. \tag{4.11}$$

The uncertainty of the Probe jet energy resolution is therefore,

$$\delta\left(\frac{\sigma_{p_T^{Probe}}}{p_T}\right) = \left[\frac{1}{\sigma_{p_T^{Probe}}/p_T}\right]\left[(\sigma_A)^2(\delta\sigma_A)^2 + \left(\frac{\sigma_{p_T^{Tag}}}{p_T}\right)^2\left(\delta\left(\frac{\sigma_{p_T^{Tag}}}{p_T}\right)\right)^2\right]^{\frac{1}{2}}. \tag{4.12}$$

The relative jet energy resolution of the Tag region $\sigma_{p_T^{Tag}}/p_T$ and its statistical uncertainty, $\delta(\sigma_{p_T^{Tag}}/p_T)$ were provided by ATLAS from the results of studies using simulated data. Table 4–2 lists the jet energy resolutions of the Tag region for each p_T^{Tag} bin which are used to determine the jet energy resolution of the Probe region.

p_T^{Tag} Bin [GeV/c]	p_T^{Tag} [GeV/c]	$\frac{\sigma\left(p_T^{Tag}\right)}{p_T}$	$\delta\left(\frac{\sigma\left(p_T^{Tag}\right)}{p_T}\right)$
20 - 40	30	0.163	$\pm$0.008
40 - 50	45	0.134	$\pm$0.007
50 - 60	55	0.123	$\pm$0.006
60 - 70	65	0.114	$\pm$0.006
70 - 80	75	0.108	$\pm$0.005
80 - 110	95	0.098	$\pm$0.005
110 - 160	135	0.087	$\pm$0.004

Table 4–2: Table of the jet energy resolutions for the Tag region used to calculate the jet energy resolutions for the Probe region with Equation 4.11. The jet energy resolutions uncertainties were provided by ATLAS through the results of studies using simulated data [1].

The standard deviation of the asymmetry distributions, σ_A, along with the statistical uncertainty, $\delta\left(\sigma_A\right)$, are obtained from the Gaussian fits of the distributions.

CHAPTER 5
Results

This chapter will discuss the results obtained by applying the analysis algorithm described in Chapter 4 to the ATLAS 2010 dataset which corresponds to approximately 35 pb^{-1} of data. This chapter begins with the description of a study to verify the validity of the analysis algorithm and motivate the η region chosen as the reference region for the Tag jet. The jet energy correction factors for the ATLAS forward calorimeters obtained and their subsequent application to data are presented in Sections 5.2 and 5.3, respectively. Section 5.4 then presents results from a brief study of the jet energy resolution of the ATLAS forward calorimeters. Finally a study of the effects of the event selection criteria on the jet energy scale and resolution ends this chapter.

5.1 Barrel Calorimeter Cross-Check

The di-jet balance method outlined in Chapter 4 was applied to the reference region within the barrel calorimeter. Both the Tag and Probe jets were required to be within the η range of $0.1<|\eta|<0.8$ and were randomly defined as the highest or second highest p_T jets in the event. To randomize the events a random number generator was used to generate a number between 0 and 1. If the number was greater than 0.5 the highest p_T jet in the event was defined to be the Tag jet and the second highest p_T jet was defined to be the Probe jet. If the number was less than 0.5 then the Tag jet was defined to be the second highest p_T jet and the Probe jet was

defined to be the highest. This randomization ensured that the Tag jet p_T was not more often larger than the Probe jet or *vice versa*. Since the barrel calorimeter is assumed to be well calibrated this serves as a good cross-check of the di-jet balance methodology.

In Section 4.2 the variances of the Tag and Probe jets were shown to have an effect on the shape and peak location of the asymmetry distributions created with Equations 4.1 and 4.2. For this study, the case where the Tag and Probe jets have the same variances, shown in Figure 4–2, was the least biased. Therefore Equation 4.2 was used for the asymmetry definition. Consequently the asymmetry distributions were binned with respect to the p_T^{Ave} of the event. The relationship between the Tag and Probe jets was found by re-arranging Equation 4.2 as follows.

$$\begin{aligned} \langle A \rangle &= \frac{p_T^{Tag} - p_T^{Probe}}{\left(p_T^{Tag} + p_T^{Probe}\right)/2} \\ \langle A \rangle \left(p_T^{Tag} + p_T^{Probe}\right) &= 2\left(p_T^{Tag} - p_T^{Probe}\right) \\ p_T^{Tag} &= \left(\frac{2 + \langle A \rangle}{2 - \langle A \rangle}\right) p_T^{Probe} \\ \langle k \rangle &= \frac{2 + \langle A \rangle}{2 - \langle A \rangle} \end{aligned} \tag{5.1}$$

In Figure 5–1 the means of the asymmetry distributions for 2−jet and $\geq 3-$jet events are shown in their respective p_T^{Ave} bins. The fitted asymmetry distributions of every p_T^{Ave} bin for the 2−jet and $\geq$ 3−jet events can be found in Figures 6–1 and 6–2 respectively in Appendix A. The 20-40 GeV/c and 40-50 GeV/c p_T bins for the $\geq$ 3−jet events were excluded because they did not have enough statistics

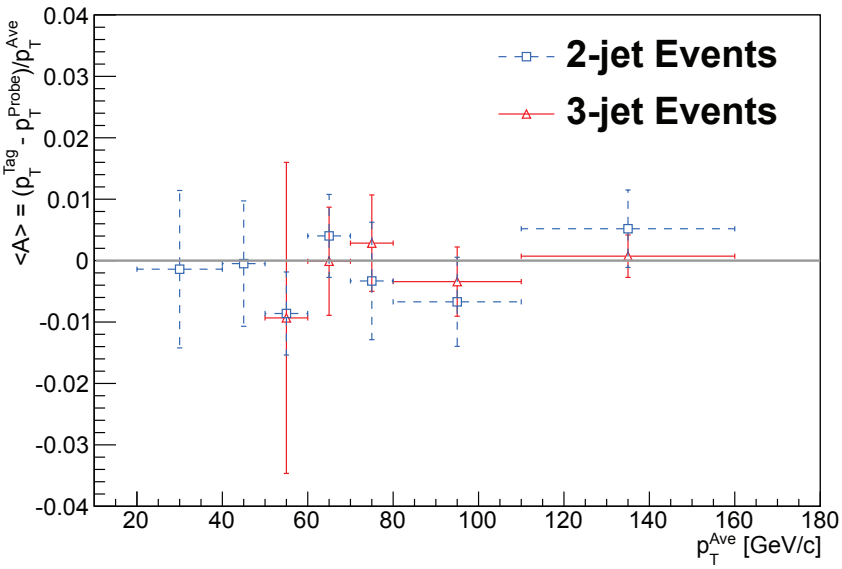

Figure 5–1: Plot of the asymmetry distribution means obtained for each p_T^{Ave} bin for 2−jet and $\geq$ 3−jet events. The vertical error bars on each point represent the statistical uncertainty on the fitted mean. The Tag and Probe jets are required to be in the η region $0.1<|\eta|<0.8$.

to provide valid Gaussian fits. The peak location for every p_T^{Ave} bin in both event samples includes $\langle A \rangle = 0$ within their statistical uncertainties. This validates the di-jet technique and also shows that the η range chosen for the reference region is properly calibrated. Any deviations away from $\langle A \rangle = 0$ for the 2−jet and $\geq$ 3−jet p_T^{Ave} bins will contribute to the systematic uncertainties for the forward calorimeter study and will be discussed in more detail in Section 5.5.1.

5.2 Determination of the Jet Energy Scale for the ATLAS Forward Calorimeters

The calibration outlined in Section 3.3 works well in theory however it is based mostly on simulated data studies and test beam results using electrons and pions.

While the forward calorimeters may perform great using test beams or simulated data, the effects of the LHC environment are hard to predict which may lead to worse performance. The difference between theory and practice means that the di-jet events passing the selection cuts may have Probe jets whose p_T differs from that of the Tag jet p_T, requiring further calibration. Figures 5–2a and 5–2b illustrate the p_T of the Tag and Probe jet for events with exactly 2−jets, and events with $\geq$ 3−jets, satisfying the event selection described in Section 4.2.1. The diagonal line indicates the ideal case where $p_T^{Tag} = p_T^{Probe}$. In both event samples, there is an obvious excess of events below the diagonal line which implies that on average $p_T^{Probe} < p_T^{Tag}$. An excess of di-jet events where the $p_T^{Probe} < p_T^{Tag}$ verifies the need for further jet energy corrections in the Probe region. The structure of the different p_T^{Tag} bins is also evident at p_T^{Tag} = 20, 40, 50, 60 and 110 GeV/c. The structure is not as evident in Figure 5–2b because of the limited statistics and how spread out the data points are. This is a consequence of the different triggers used for these p_{Tag} ranges. The separation between adjacent p_T^{Tag} bins at 70 and 80 GeV/c do not exhibit the same type of structure because the same trigger is used to populate all three bins from 60 to 110 GeV/c.

Figure 5–3 shows the means of the asymmetry distributions for 2−jet and $\geq$ 3−jet events as a function of p_T^{Tag}. The fitted asymmetry distributions of every p_T^{Tag} bin for the 2−jet and $\geq$ 3−jet events can be found in Figures 6–3 and 6–4 respectively in Appendix A. As expected from the trend shown in Figures 5–2a and 5–2b, the asymmetry means are shifted on the positive side away from $\langle A \rangle = 0$. For every p_T^{Tag} bin the 2−jet events are closer to $\langle A \rangle = 0$ than the $\geq$ 3−jet events. A better

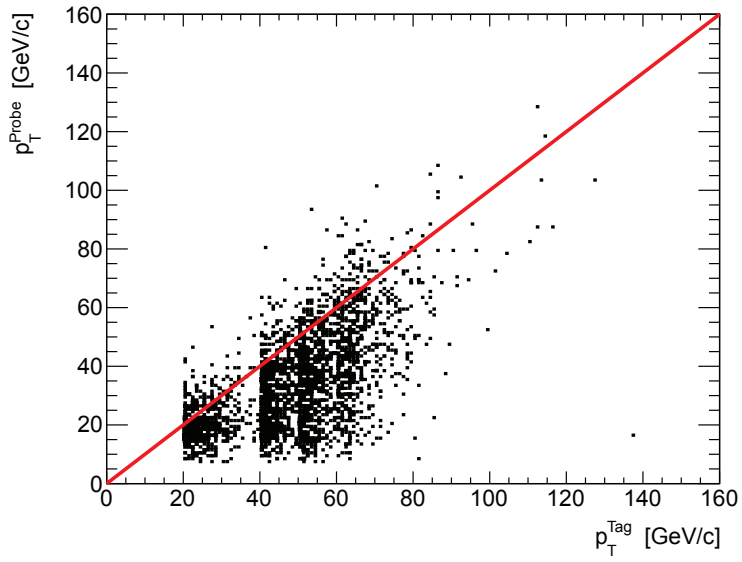

(a) 2−jet events.

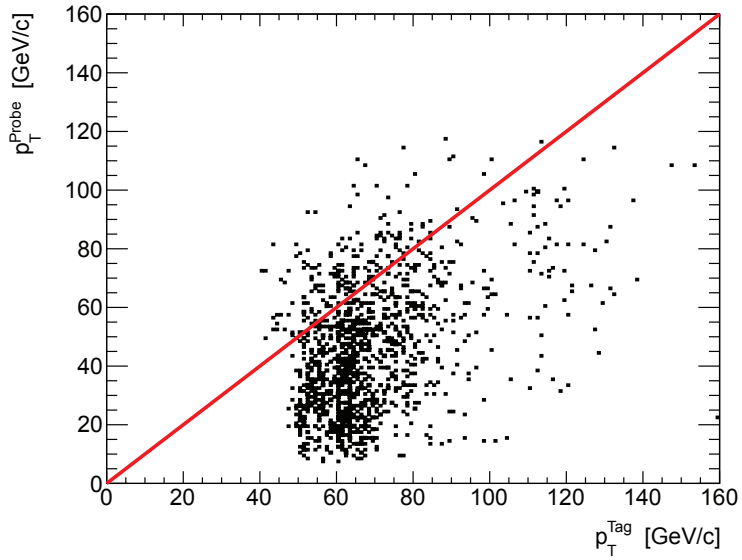

(b) $\geq$ 3−jet events

Figure 5–2: Scatter plot of the Tag and Probe jet p_T for (a) 2−jet and (b) $\geq$ 3−jet events which have passed the selection cuts outlined in Section 4.2.1. The line represents when $p_T^{Tag} = p_T^{Probe}$.

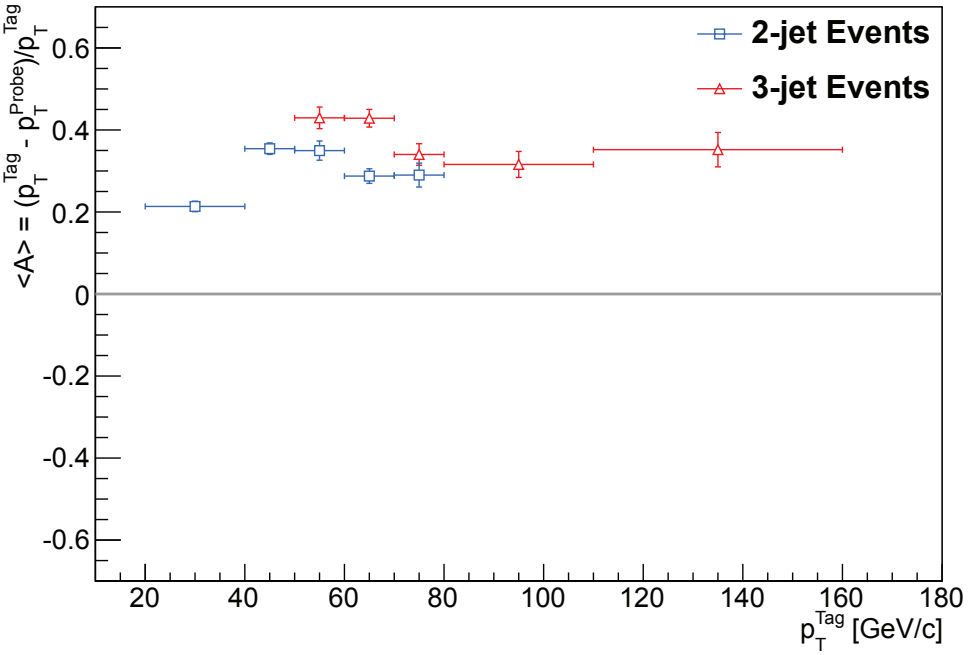

Figure 5–3: Diagram of the asymmetry distribution means obtained for each p_T^{Tag} bin for 2−jet and $\geq$ 3−jet events. The vertical error bars on each point represent the statistical uncertainty on the fitted mean. The Tag and Probe jets were required to be within the $|\eta|$ regions $0.1 < |\eta| < 0.8$ and $3.6 < |\eta| < 4.6$, respectively. The p_T^{Tag} bins from 20-50 GeV/c for the $\geq$ 3−jet events and 80-110 GeV/c for the 2−jet events did not have sufficient enough statistics to fit so they were excluded.

balance for 2−jet events is expected because they do not have any other jets that may contribute to a p_T imbalance in the event. Table 5–1 lists the correction factors and their uncertainties obtained using 2−jet and $\geq$ 3−jet events which were calculated using Equations 4.8 and 4.9 respectively. The correction factors for the 2−jet and $\geq$ 3−jet events do not agree within their uncertainties for most p_T^{Tag} bins. This could be caused by the extra jet in the event or due to the limited amount of statistics available for each p_T^{Tag} bin. Therefore the 2−jet and $\geq$ 3−jet events were further analyzed separately and not merged.

p_T^{Tag} Bin [GeV/2]	2−Jet Events		$\geq$ 3-Jet Events	
	Correction Factor (k)	Statistical Error	Correction Factor (k)	Statistical Error
20 - 40	1.27	0.02	N/A	N/A
40 - 50	1.55	0.03	N/A	N/A
50 - 60	1.54	0.06	1.75	0.08
60 - 70	1.40	0.04	1.75	0.07
70 - 80	1.41	0.06	1.52	0.06
80 - 110	1.29	0.07	1.46	0.07
110 - 160	N/A	N/A	1.5	0.1

Table 5–1: Table of the correction factors found for 2−jet and $\geq$ 3−jet events for each p_T^{Tag} bin. The Tag and Probe jets were required to be within the $|\eta|$ regions $0.1 < |\eta| < 0.8$ and $3.6 < |\eta| < 4.6$, respectively. The "N/A" entry means that no fit was obtained for that sample and p_T^{Tag} bin due to insufficient statistics. The statistical error was calculated using Equation 4.9 from Section 4.2.3.

5.3 Application of the Correction Factors

The effects of applying the correction factors listed in Table 5–1 to the data are explored in this section. For events that passed the selection criteria, the correction factor corresponding to the p_T of the Tag jet for that event was applied to the Probe

jet p_T as per Equation 4.7. The di-jet balance method was then re-applied to the Tag and p_T-corrected Probe jet.

Figures 5–4a and 5–4b depict the p_T^{Tag} versus p_T^{Probe} spectrum for the corrected di-jet events. As expected, when compared to Figures 5–2a and 5–2b, the events are more evenly distributed about the diagonal line which implies that a better overall balance has been achieved. It is also apparent that the p_T^{Probe} spectrum is significantly wider for each of the p_T^{Tag} bins. The smearing of the asymmetry distributions is a consequence of applying one correction factor for a range of p_T^{Tag} values. The peak regions of the distributions will be shifted to or close to 0 however the entries in the tails of the distributions will be shifted to a position further away from the peak than before the application of the correction factors. The fact that one correction factor is applied to a range of p_T^{Tag} values also explains why the balance or $\langle A \rangle$ values shown in Figure 5–5 for the corrected asymmetry distributions are not identically zero.

Figure 5–5 illustrates the mean of the corrected asymmetry distributions for 2−jet and $\geq$ 3−jet events. The fitted asymmetry distributions of every p_T^{Tag} bin for the corrected 2−jet and $\geq$ 3−jet events can be found in Figures 6–5 and 6–6 respectively in Appendix A. As expected the mean of the corrected asymmetry for both 2-jet and >= 3-jet events for every p_T^{Tag} bin agrees with 0 to within statistical uncertainties. Therefore the application of the correction factors has improved the energy response of the forward calorimeters.

5.4 Jet Energy Resolution Before the Application of the Correction Factors

A brief study of the jet energy resolution of the forward calorimeters before the correction factors were applied will be explored in this section using the techniques

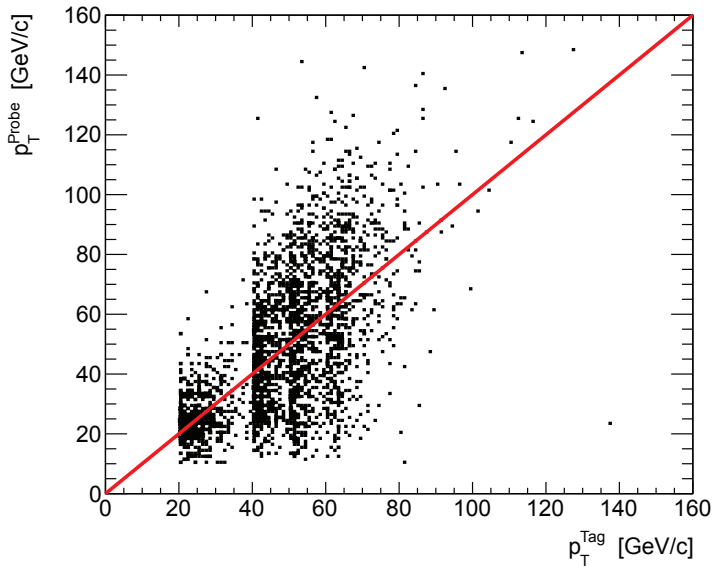

(a) 2−jet events.

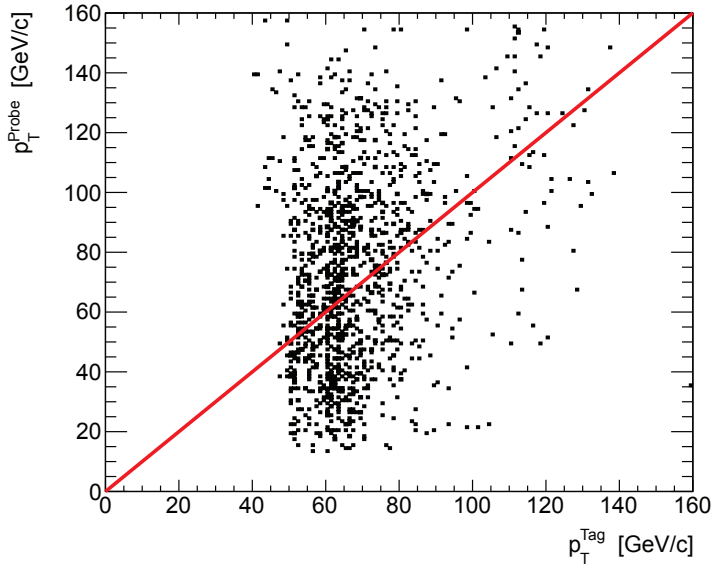

(b) $\geq$ 3−jet events

Figure 5–4: Scatter plot of the Tag and corrected Probe jet p_T for (a) 2−jet and (b) $\geq$ 3−jet events which have passed the selection cuts outlined in Section 4.2.1. Probe jets are corrected with the factors listed in Table 5–1. The line represents when $p_T^{Tag} = p_T^{Probe}$.

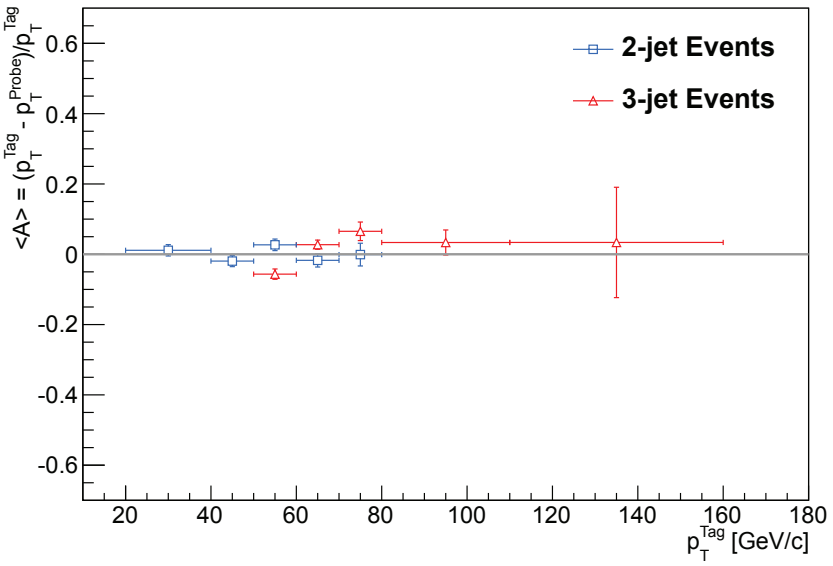

Figure 5–5: Diagram of the asymmetry distribution means obtained for each p_T^{Tag} bin for 2−jet and $\geq$ 3−jet events after applying the Probe jet correction factors listed in Table 5–1. The vertical error bars on each point represent the statistical uncertainty on the fitted mean. The Tag and Probe jets were required to be within the $|\eta|$ regions $0.1 < |\eta| < 0.8$ and $3.6 < |\eta| < 4.6$, respectively.

outlined in Section 4.2.4. The jet energy resolution and statistical uncertainty was calculated for every p_T^{Tag} bin using Equations 4.11 and 4.12, respectively. Table 5–2 lists the results of these calculations for the 2−jet and $\geq$ 3−jet event asymmetry distributions. The resolution term for the 20-40 GeV/c bin of the 2−jet event sample is uncharacteristically low and does not follow the general trend of the parametric equation for the jet energy resolution defined by Equation 3.6. Figure 6–3a in Appendix A shows the Gaussian fit corresponding to this p_T^{Tag} bin. The chi-square per number of degrees of freedom for this bin is larger than 2 which suggests that the single Gaussian distribution does not adequately represent the distribution of the

p_T^{Tag} Bin (GeV/c)	2-Jet Events		$\geq$ 3-Jet Events	
	$\frac{\sigma(p_T^{Probe})}{p_T}$	$\delta\left(\frac{\sigma(p_T^{Probe})}{p_T}\right)$	$\frac{\sigma(p_T^{Probe})}{p_T}$	$\delta(\frac{\sigma(p_T^{Probe})}{p_T})$
20 - 40	0.16	0.02	N/A	N/A
40 - 50	0.23	0.02	N/A	N/A
50 - 60	0.34	0.04	0.25	0.04
60 - 70	0.25	0.02	0.33	0.02
70 - 80	0.18	0.04	0.24	0.03
80 - 110	0.12	0.09	0.20	0.05
110 - 160	N/A	N/A	0.14	0.07

Table 5–2: Table of jet energy resolution and statistical uncertainty for 2−jet and $\geq$ 3−jet events for each p_T^{Tag} bin. The "N/A" entry means that no fit was obtained for that sample and p_T^{Tag} bin due to insufficient statistics. The uncertainty on the jet energy resolution was calculated using Equation 4.12 from Section 4.2.4.

data. The results are therefore less reliable than in other fits where a single Gaussian seems to more appropriately describe the data. This is a limitation of fitting a single Gaussian to the peak region of a distribution. Future work may consider using a double Gaussian to better fit the asymmetry distributions. Therefore the 20-40 GeV/c bin of the 2−jet event sample was excluded from further resolution analysis.

The jet energy resolution listed in Table 5–2 were fit using only the stochastic term of Equation 3.6 given by,

$$\frac{\sigma_{p_T}}{p_T} = \frac{S}{\sqrt{p_T}}. \tag{5.2}$$

The constant and noise terms were left out because of the limited p_T range of the events in this analysis and the small number of data points to fit. Figure 5–6 depicts the jet energy resolution for the 2−jet and $\geq$ 3−jet events along with their respective fits. In general the jet energy resolution for the 2−jet events is better than that of the $\geq$ 3−jet events. This was expected considering that the $\geq$ 3−jet events are only

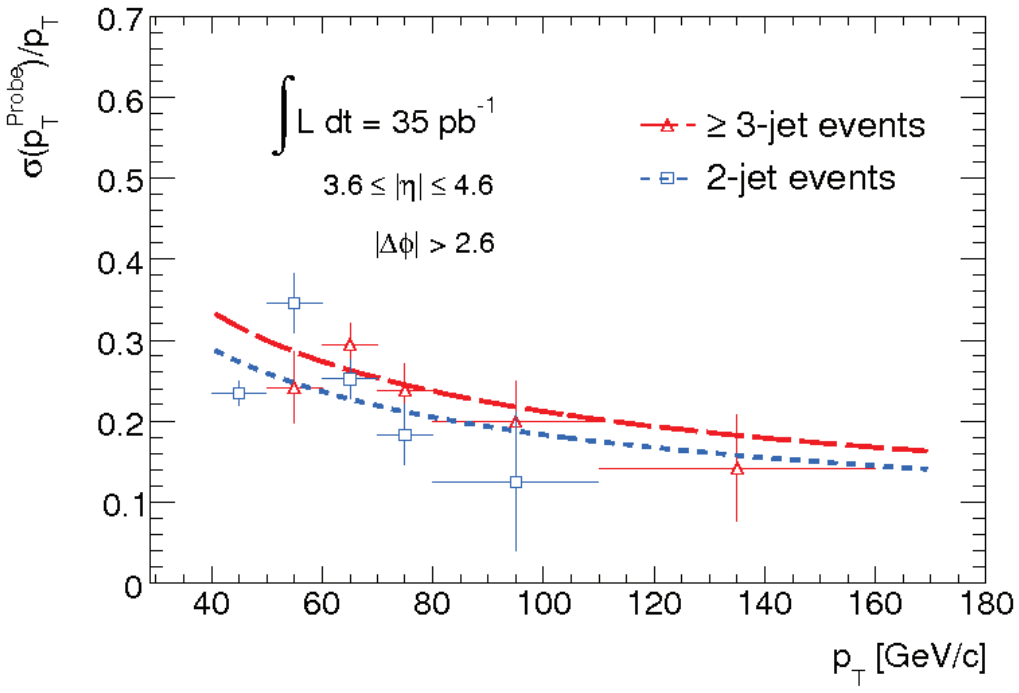

Figure 5–6: Diagram of the jet energy resolution and statistical uncertainty listed in Table 5–2 for 2−jet and ≥ 3−jet events fit with Equation 5.2. The vertical error bars on each point represent the statistical uncertainty calculated with Equation 4.12.

approximate di-jet events with a third jet that can contribute to the variance of the probe jet energy. The stochastic terms obtained from the fits shown in Figure 5–6 are listed in Table 5–3. Table 5–3 also shows the σ_{p_T} for a 30 GeV/c jet calculated from the corresponding stochastic term, S using Equation 5.2. The last column in Table 5–3 shows the current estimate of σ_{p_T} for a 30 GeV/c jet in the forward calorimeter [2]. All of the calculated values for σ_{p_T} for a 30 GeV/c jet agree within their uncertainties. Therefore the stochastic terms found for the 2−jet and ≥ 3−jet events are acceptable estimates for the forward calorimeters.

Sample	Stochastic Term (S) $[\%\sqrt{\text{GeV/c}}]$	Calculated $\sigma^{Probe}_{p_T=30\,\text{GeV/c}}$ (GeV/c)	Estimated $\sigma^{Probe}_{p_T=30\,\text{GeV/c}}$ (GeV/c)
2−jet	180 ± 11	9.9 ± 0.6	~ 10
≥ 3−jet	210 ± 15	11.5 ± 0.8	~ 10

Table 5–3: Table of the stochastic terms for 2−jet and ≥ 3−jet event obtained from fits found in Figure 5–6. The uncertainty on the stochastic terms is statistical and was obtained from fits found in Figure 5–6. The last two columns are the calculated and current estimate of the jet energy resolution for a 30 GeV/c jet in the Probe region [2]. The calculated jet energy resolution was determined by using Equation 5.2 with the stochastic terms from the second column. The uncertainty was calculated using the general rule for error propagation [3].

5.5 Systematic Considerations

This section will discuss the systematic uncertainties considered in this analysis, which consist of quantifying the effect of variations in the selection cuts applied: the balance of the Tag region, how back-to-back the Tag and Probe jets are, the minimum jet p_T threshold at the EM-scale and finally the maximum p_T allowed for a third jet.

5.5.1 Di-Jet Balancing within the Barrel Calorimeter

In order to determine proper correction factors for the forward calorimeter using the di-jet balance method, the reference region that is used must be properly calibrated. In Section 5.1 the balance of the reference region within the barrel calorimeter itself was investigated. The correction factors were calculated using Equation 5.1 and the asymmetry distribution means found in Figure 5–1. Similar to the asymmetry distributions, the correction factors in each p_T^{Tag} bin are within $\sim 1\%$ of a perfect balance of 0. These slight deviations from $k_{Ave} = 1$ are included in the systematic errors for the 2−jet and ≥ 3−jet events listed in Tables 5–5 and 5–6 respectively.

5.5.2 Jet $p_T^{EMscale}$ Threshold

The minimum jet p_T cut at the electromagnetic scale prevents improperly calibrated low p_T jets from biasing the results. Figures 5–7a and 5–7b show the variation of the correction factors (k) for each p_T^{Tag} bin of the 2−jet and ≥ 3−jet events for minimum jet $p_T^{EMscale}$ cuts of 5, 10 and 15 GeV/c. A 5 GeV/c variation on the threshold was chosen as a reasonable estimate of the jet p_T resolution at the electromagnetic scale. Varying this cut appears to have the most significant effect on the correction factors in the low p_T bins, namely < 60 GeV/c for the 2−jet events and < 70 GeV/c for the ≥ 3−jet events. As the minimum jet $p_T^{EMscale}$ cut increases, the correction factors in Figures 5–7a and 5–7b for each p_T^{Tag} bin decrease towards $k = 1$. The deviations from the correction factors obtained from the nominal minimum jet $p_T^{EMscale}$ cut of 10 GeV/c for the 2−jet and ≥ 3−jet events are summarized in Tables 5–5 and 5–6 respectively.

The jet energy resolution for each p_T^{Tag} bin of the 2−jet and ≥ 3−jet events was also found for each variation of the minimum jet $p_T^{EMscale}$ cut. Results obtained with each variation of the jet $p_T^{EMscale}$ cut were fitted using Equation 5.2 to determine a value for the stochastic term. Figures 5–8a and 5–8b depict the jet energy resolution for each variation of the minimum jet $p_T^{EMscale}$ cut and the fits for the 2−jet and ≥ 3−jet events respectively. In both the 2−jet and ≥ 3−jet events, the stochastic term from Equation 5.2 decreased as the minimum jet $p_T^{EMscale}$ cut was varied from 5 GeV/c to 10 GeV/c and then finally to 15 GeV/c. Table 5–7 lists the stochastic fit parameter for the 2−jet and ≥ 3−jet events along with the deviations due to variations in the minimum jet $p_T^{EMscale}$ cut. It is apparent that the minimum jet

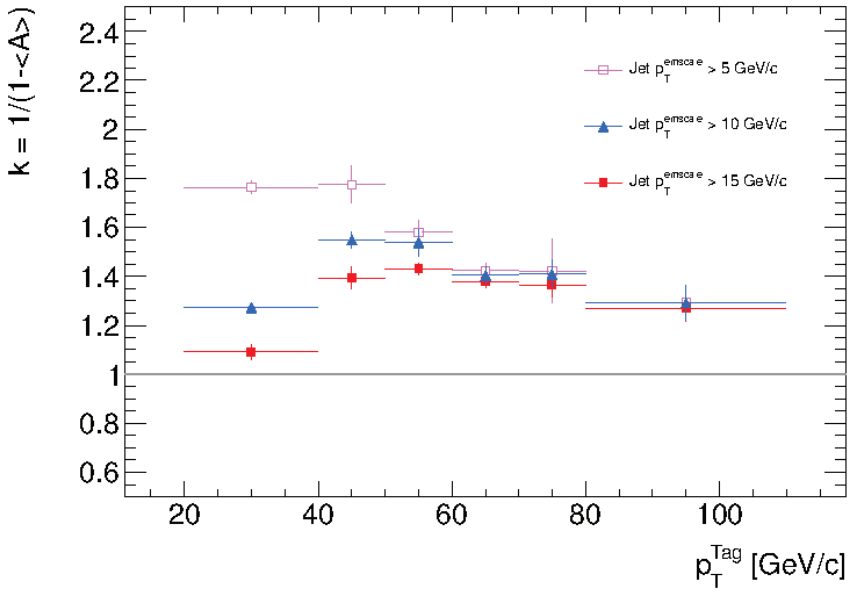

(a) 2−jet events.

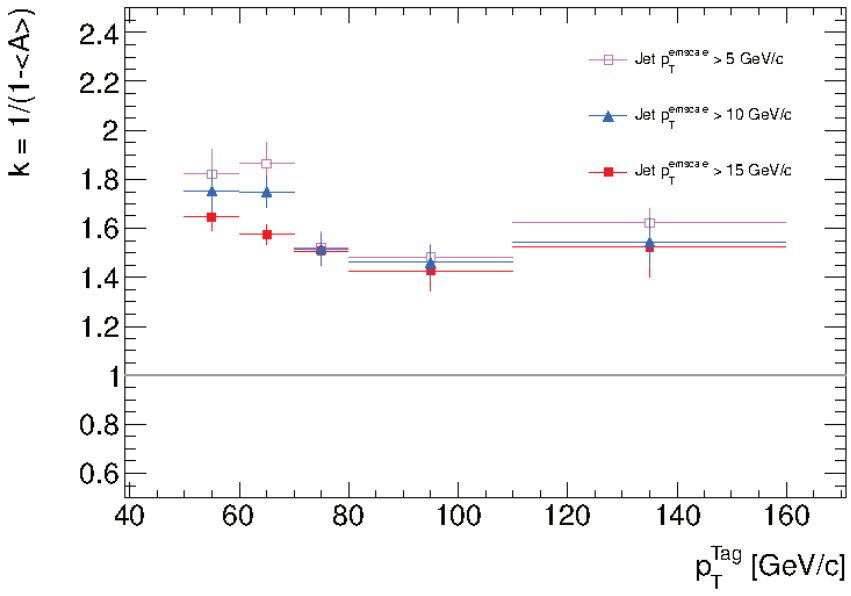

(b) ≥ 3−jet events.

Figure 5–7: Comparison of the correction factors for (a) 2−jet and (b) ≥ 3−jet events vs p_T^{Tag} for cuts on the minimum jet $p_T^{EMscale}$ of 5, 15 and the nominal cut of 10 GeV/c using the full ATLAS 2010 data-set. The vertical error bars on each point represent the statistical uncertainty calculated with Equation 4.9.

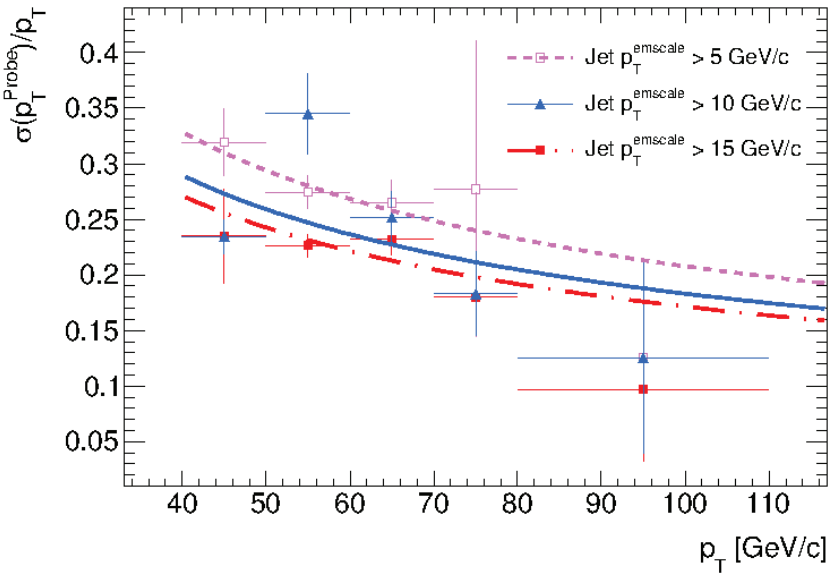

(a) 2−jet events.

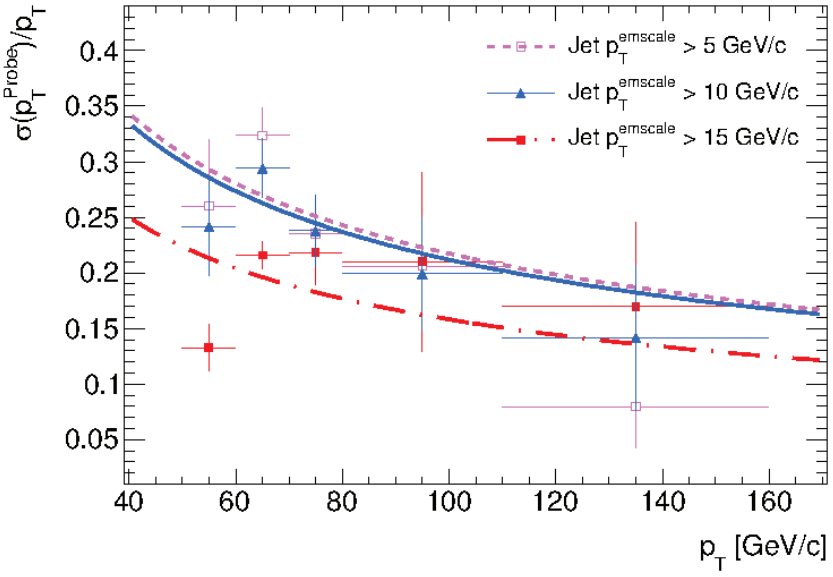

(b) $\geq$ 3−jet events

Figure 5–8: Comparison of the jet energy resolution for (a) 2−jet and (b) $\geq$ 3−jet events vs p_T for cuts on the minimum jet $p_T^{EMscale}$ of 5, 15 and the nominal cut of 10 GeV/c using the full ATLAS 2010 data-set. Each cut variation is fitted with Equation 5.2. The vertical error bars on each point represent the statistical uncertainty calculated with Equation 4.12.

$p_T^{EMscale}$ cut variation of 15 GeV/c has a much larger effect on the jet energy resolution than the cut variation of 5 GeV/c for the $\geq 3-$jet events. A reason for this could be that by decreasing/increasing this cut one allows more/less improperly calibrated, low p_T jets in which can contribute to the variance or width of the asymmetry distributions.

5.5.3 $|\Delta\phi|$ Cut

The $|\Delta\phi|$ cut was varied by 0.3 radians around the nominal cut of 2.6 radians. The variation of 0.3 radians was chosen based on half of the uncertainty on the $|\Delta\phi|$ cut defined in Section 4.2.1. The correction factors for the 2−jet and $\geq 3-$jet events are depicted in Figures 5–9a and 5–9b respectively, with the $|\Delta\phi|$ cut varied between 2.3, 2.6, and 2.9 radians. Figures 5–9a and 5–9b show that as the $|\Delta\phi|$ cut is tightened the correction factors for each p_T^{Tag} bin decrease closer to $k = 1$. This is expected because by tightening the $|\Delta\phi|$ cut the events are forced to be more and more back-to-back and therefore more balanced with correction factors closer to $k = 1$.

Figures 5–10a and 5–10b show the effects of the varied $|\Delta\phi|$ cut on the jet energy resolution of the probe jet for 2−jet and $\geq 3-$jet events. Varying the $|\Delta\phi|$ cut did not significantly affect the stochastic fit results for the $\geq 3-$jet events. In both the 2−jet and $\geq 3-$jet events an increase in the $|\Delta\phi|$ cut corresponded to a decrease in the stochastic energy resolution term. The stochastic term fit from the 2−jet events was the only sample significantly affected by the $|\Delta\phi| > 2.3$ variation which resulted in an absolute increase of the stochastic term by about 0.27 $\sqrt{\text{GeV/c}}$.

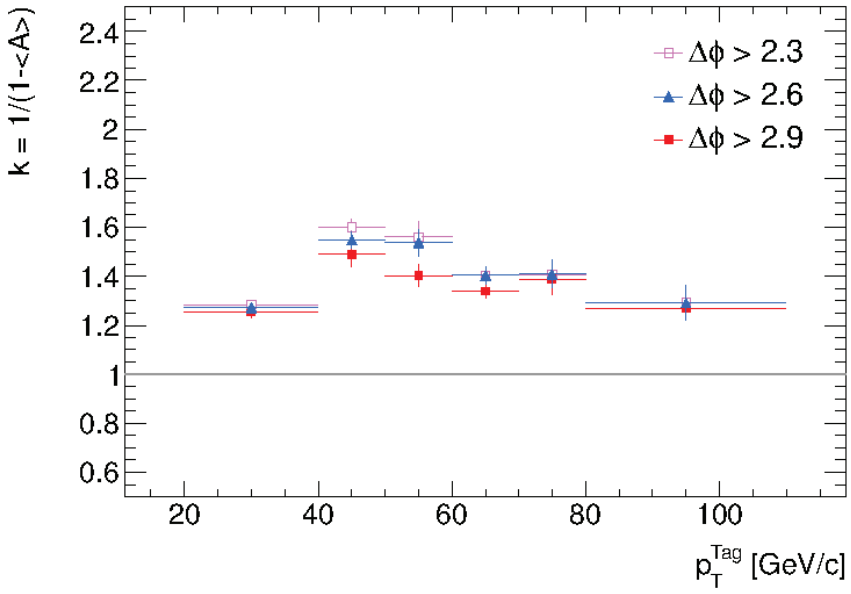

(a) 2−jet events.

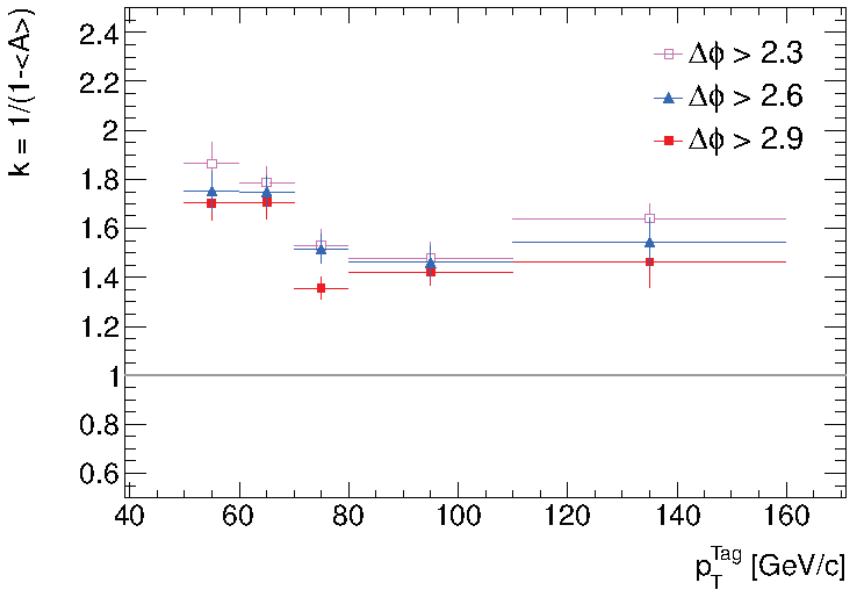

(b) ≥ 3−jet events

Figure 5–9: Comparison of the correction factors for (a) 2−jet and (b) ≥ 3−jet events vs p_T^{Tag} for $|\Delta\phi|$ cut values of 2.3, 2.9 and the nominal cut of 2.6 radians between the Tag and Probe jets using the full ATLAS 2010 data-set. The vertical error bars on each point represent the statistical uncertainty calculated with Equation 4.9.

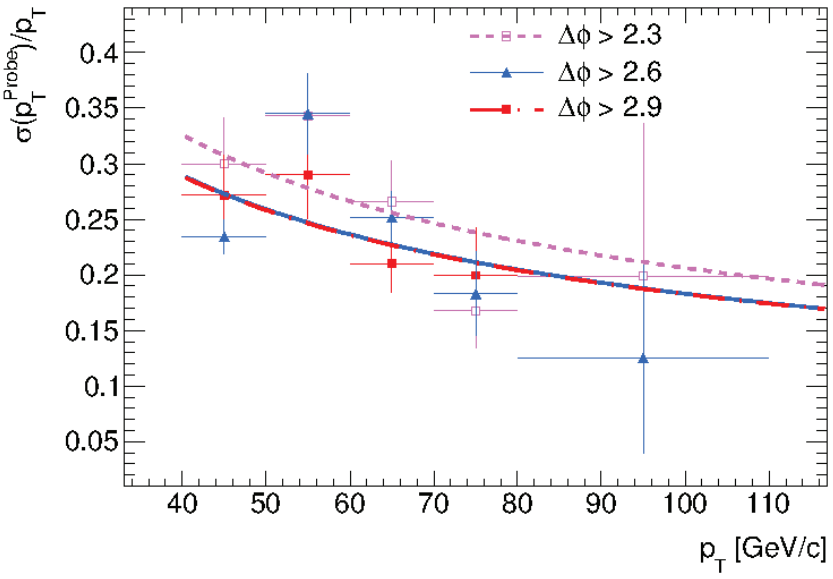

(a) 2−jet events.

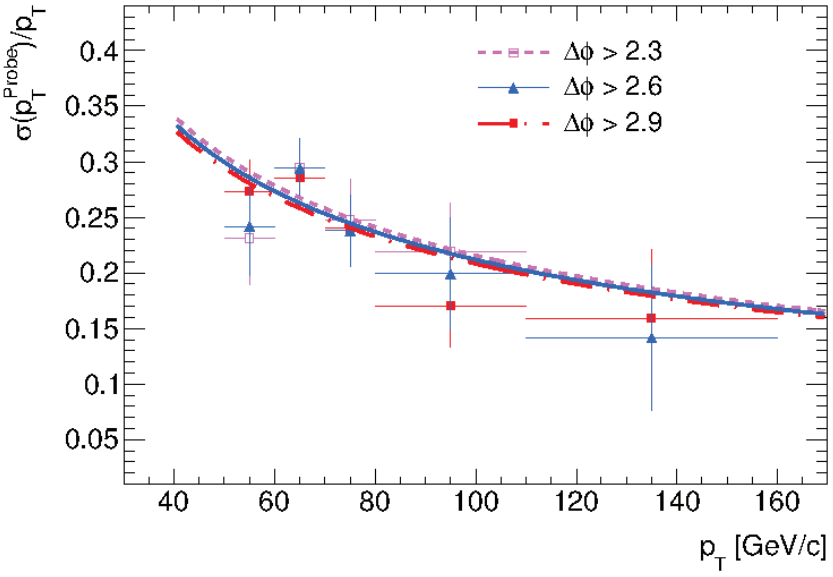

(b) ≥ 3−jet events

Figure 5–10: Comparison of the jet energy resolution for (a) 2−jet and (b) ≥ 3−jet events vs p_T for $|\Delta\phi|$ cut values of 2.3, 2.9 and the nominal cut of 2.6 radians between the Tag and Probe jets using the full ATLAS 2010 data-set. Each cut variation is fitted with Equation 5.2. The vertical error bars on each point represent the statistical uncertainty calculated with Equation 4.12.

An increase in resolution is expected when loosening the $|\Delta\phi|$ cut because events that are not truly back-to-back are being accepted which will cause more variance in the asymmetry distributions.

5.5.4 Third Jet Effects

The effect of the third jet p_T cut on the correction factors and jet energy resolution of the probe region for the $\geq 3-$jet events was also investigated by varying F_3, defined by Equation 4.5, from 11% to 15% and 19%. Figure 5–11 depicts the distribution of F_3 for the $\geq 3-$jet events which satisfied the selection cuts outlined in Section 4.2.1 except for the $|\Delta\phi|$ and trigger cuts. The nominal cut of $F_3 = 15\%$ is shown by the red vertical line and the variation cuts of $F_3 = 11\%$ and 19% are shown by the blue lines. The cuts of 11% and 19% were chosen to span either side of the peak around 15%.

The amount of statistics decreased dramatically for the $F_3 = 11\%$ variation such that there were not enough entries in the p_T^{Tag} bins to warrant proper Gaussian fits. Therefore a rough estimate of the uncertainty on this cut was determined by combining all of the p_T^{Tag} bins and comparing the total asymmetry distributions for each variation of the third jet p_T cut. Table 5–4 lists the total asymmetry correction factors and their uncertainties for $\geq 3-$jet events where $F_3 = 11\%$, 15% and 19%. The correction factors vary by about $\pm$0.25-0.30 from the nominal third jet p_T cut of $F_3 = 15\%$.

Table 5–4 also lists the resolution terms for the total asymmetry distributions when F_3 was varied from 11%, 15%, and 19%. Since a proper fit could not have been made on one data point, the deviations of the resolution from the nominal cut

were taken to be a crude estimate of the size of this systematic uncertainty on the stochastic term of the jet energy resolution.

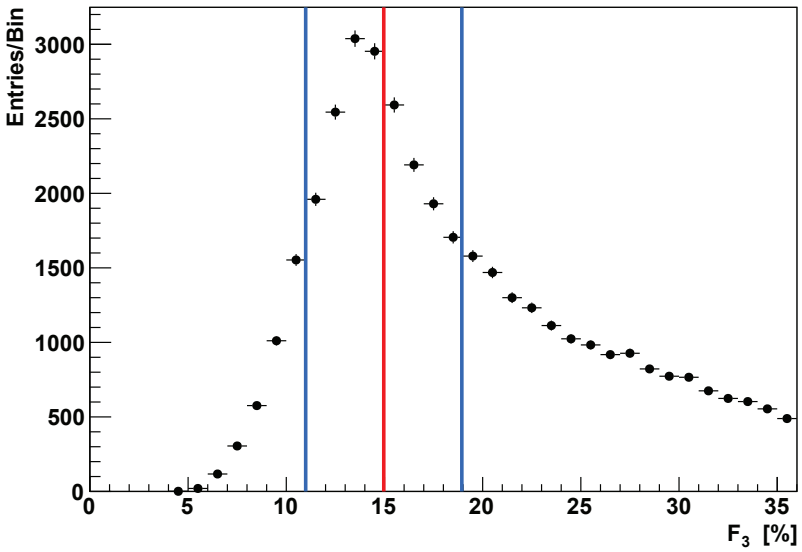

Figure 5–11: The distribution of F_3 for the $\geq 3-$jet events which satisfy the selection cuts outlined in Section 4.2.1 except for the $|\Delta\phi|$ and trigger cuts. The vertical lines represent the varied cuts of 11% 15% and 19%. The vertical error bars are purely statistical.

$p_T^{3^{rd}Jet}$ Cut (GeV/c)	k	δk	$\frac{\sigma\left(p_T^{Probe}\right)}{p_T}$	$\delta\left(\frac{\sigma\left(p_T^{Probe}\right)}{p_T}\right)$
11	1.34	± 0.07	0.22	± 0.06
15	1.65	± 0.04	0.28	± 0.02
19	1.84	± 0.06	0.34	± 0.05

Table 5–4: Table of correction factors and jet energy resolution terms for the combined $\geq 3-$jet events asymmetry distributions for values of $F_3 = 11\%$, 19% and the nominal cut of 15% using the full ATLAS 2010 data-set. The uncertainties for the correction factors and jet energy resolution terms are statistical and calculated with Equations 4.9 and 4.12 respectively.

Both the correction factors k, and the stochastic energy resolution terms increased when the F_3 cut was increased. This is an expected trend because when F_3 increases, events with larger or more significant third jet p_T are accepted into the "di-jet" sample. This causes an imbalance between the Tag and Probe jets which translates into asymmetry distributions with $\langle A \rangle \neq 0$.

5.5.5 Combining the Systematic Uncertainties

Tables 5–5 and 5–6 summarize the systematic contributions to the correction factor uncertainties considered in this section for the 2−jet and $\geq 3-$jet events respectively. The last columns in both tables show the total uncertainties for each p_T^{Tag} bin obtained by adding all systematic and statistical contributions together in quadrature. The minimum jet $p_T^{EMscale}$ cut and statistical uncertainty are the dominant sources of uncertainty for the 2−jet events correction factors. The dominant source of error on the correction factors for the $\geq 3-$jet events was the third jet p_T cut. The rest of the systematic considerations for the $\geq 3-$jet events contribute on average, equally to the correction factor uncertainty. Table 5–7 lists the results from the jet energy resolution fits to the stochastic term for the 2−jet and $\geq 3-$jet events as well as the size of uncertainties for each source considered. The last column represents all the systematic and statistical uncertainties added together in quadrature. The largest contributor to the stochastic term uncertainty is the minimum jet $p_T^{EMscale}$ cut.

This thesis has investigated the jet energy scale and resolution of the ATLAS forward calorimeters using di-jet balancing. In general the current calibration applied to the forward calorimeters needs to be improved. The derived correction factors

p_T^{Tag} Bin (GeV/c)	k	Summary of Uncertainties: Statistical Error	Jet $p_T^{EMscale}$	$\|\Delta\phi\|$	Barrel Cross Check	Combined
20 - 40	1.27	± 0.02	$^{+0.50}_{-0.20}$	$^{+0.01}_{-0.01}$	± 0.001	$^{+0.50}_{-0.20}$
40 - 50	1.55	± 0.03	$^{+0.20}_{-0.20}$	$^{+0.05}_{-0.06}$	± 0.0007	$^{+0.21}_{-0.21}$
50 - 60	1.54	± 0.06	$^{+0.05}_{-0.11}$	$^{+0.02}_{-0.14}$	± 0.01	$^{+0.08}_{-0.19}$
60 - 70	1.40	± 0.04	$^{+0.01}_{-0.03}$	$^{+0.003}_{-0.07}$	± 0.006	$^{+0.04}_{-0.09}$
70 - 80	1.41	± 0.06	$^{+0.01}_{-0.04}$	$^{+0.007}_{-0.03}$	± 0.004	$^{+0.06}_{-0.08}$
80 - 110	1.29	± 0.07	$^{+0.00}_{-0.03}$	$^{+0.00}_{-0.03}$	± 0.009	$^{+0.07}_{-0.08}$
110 - 160	N/A	N/A	N/A	N/A	N/A	N/A

Table 5–5: Table of the correction factors for 2−jet events along with a summary of the statistical and systematic errors associated with each p_T^{Tag} bin. The 110-160 p_T^{Tag} bin does not have results because there weren't enough statistics to warrant a suitable Gaussian fit. Jets were reconstructed using the anti-kt algorithm and have passed all of the jet selection criteria.

p_T^{Tag} Bin (GeV/c)	k	Summary of Uncertainties: Statistical Error	Jet $p_T^{EMscale}$	$\|\Delta\phi\|$	Barrel Cross Check	$p_T^{3rd\,Jet}$	Combined
20 - 40	N/A	N/A	N/A	N/A	N/A	N/A	N/A
40 - 50	N/A	N/A	N/A	N/A	N/A	N/A	N/A
50 - 60	1.75	± 0.08	$^{+0.07}_{-0.11}$	$^{+0.11}_{-0.53}$	± 0.02	$^{+0.33}_{-0.19}$	$^{+0.36}_{-0.58}$
60 - 70	1.75	± 0.07	$^{+0.12}_{-0.18}$	$^{+0.04}_{-0.04}$	± 0.002	$^{+0.33}_{-0.19}$	$^{+0.36}_{-0.27}$
70 - 80	1.52	± 0.06	$^{+0.01}_{-0.02}$	$^{+0.02}_{-0.17}$	± 0.005	$^{+0.29}_{-0.17}$	$^{+0.30}_{-0.25}$
80 - 110	1.46	± 0.07	$^{+0.01}_{-0.04}$	$^{+0.01}_{-0.04}$	± 0.004	$^{+0.28}_{-0.16}$	$^{+0.29}_{-0.18}$
110 - 160	1.50	± 0.10	$^{+0.08}_{-0.02}$	$^{+0.09}_{-0.08}$	± 0.001	$^{+0.29}_{-0.17}$	$^{+0.33}_{-0.21}$

Table 5–6: Table of the correction factors for $\geq$ 3−jet events along with a summary of the statistical and systematic errors associated with each p_T^{Tag} bin. The 20-40 and 40-50 p_T^{Tag} bins do not have results because they did not have enough statistics to warrant a suitable Gaussian fits. Jets were reconstructed using the anti-kt algorithm and have passed all of the jet selection criteria.

Sample	S [$\%\sqrt{\text{GeV/c}}$]	Summary of Uncertainties [$\%\sqrt{\text{GeV/c}}$]				
		Statistical Error	Jet $p_T^{EMscale}$	$\lvert\Delta\phi\rvert$	$p_T^{3^{rd}Jet}$	Combined
2−jet	180	± 11	$^{+25}_{-11}$	$^{+27}_{-1}$	N/A	$^{+38}_{-16}$
$\geq 3-$jet	210	± 15	$^{+6}_{-53}$	$^{+4}_{-4}$	$^{+45}_{-45}$	$^{+48}_{-71}$

Table 5–7: Table of the stochastic jet energy resolution terms for 2−jet and $\geq 3-$jet events along with a summary of the statistical and systematic errors. Jets were reconstructed using the anti-kt algorithm and have passed all of the jet selection criteria.

were shown to improve the jet energy scale of the forward calorimeters by providing a better balance within the various p_T^{Tag} bins for the 2−jet and $\geq 3-$jet di-jet events. The stochastic term of the jet energy resolution was also determined and shown to agree with expected values as in Table 5–3. Furthermore, a systematic study was performed on the event selection cuts and other possible sources of uncertainties. This revealed that the minimum jet $p_T^{EMscale}$ cut and the third jet p_T cut were the largest sources of uncertainty.

CHAPTER 6
Conclusions

A detailed study of the performance of the ATLAS forward calorimeters has been presented in this thesis. This analysis used the full ATLAS 2010 data-set which corresponds to an integrated luminosity of $\sim$35 pb^{-1}. The di-jet balance technique was used to test the current jet energy scale and determine possible correction factors for transverse momenta bins ranging from 20 GeV/c to 160 GeV/c for 2−jet and $\geq$ 3−jet events. The stochastic term for the jet energy resolution for the 2−jet and $\geq$ 3−jet events was also determined using the di-jet balance technique.

All of the asymmetry distribution means in the $|\eta|$ range $3.6 < |\eta| < 4.6$ within the forward calorimeters deviated by $\sim 40\%$ from a well-calibrated value of zero. The application of the calculated corrections factors restored the asymmetry distribution means for both the 2−jet and $\geq$ 3−jet events to zero within statistical uncertainties. This implies that the current jet energy scale is insufficient in the forward calorimeter region and needs improvement. The stochastic terms of the jet energy resolution were found to be $\left(180^{+38}_{-16}\right)\%\sqrt{GeV/c}$ for 2−jet events and $\left(210^{+48}_{-71}\right)\%\sqrt{GeV/c}$ for $\geq$ 3−jet events. These estimates agree within statistical uncertainty with the current measured values in ATLAS.

The systematic study showed that the largest contributor to the uncertainty in the correction factors for the 2−jet events is the minimum jet p_T cut. The low p_T^{Tag} bins were affected the most by the variations on this cut. This is understandable

considering that when this cut is increased, less jets are available for the low p_T^{Tag} bins making the distribution harder to fit. If the cut is decreased, then more low, possibly poorly calibrated $p_T^{EMscale}$ jets are available which will bias or offset the peak location of the distribution. The uncertainty in the correction factors for the $\geq$ 3−jet events were affected the most by the third jet p_T cut. Since only the total asymmetry distributions were analyzed for this systematic consideration, this systematic uncertainty may be a drastic overestimation. In order to be able to apply these types of correction factors to the ATLAS calibration, consistent values between the 2−jet and $\geq$ 3−jet event samples must be demonstrated. Consistency between the energy resolution terms of the 2−jet and $\geq$ 3−jet event samples can be improved by applying a technique to the $\geq$ 3−jet event sample to compensate for the existence of higher order jets. To implement this technique asymmetry distributions for every p_T^{Tag} bin are found for several F_3 values. A linear relationship between the energy resolution and the F_3 cut for each p_T^{Tag} bin can be determined and extrapolated to $F_3 = 0$. The extrapolated energy resolution when $F_3 = 0$ should be consistent with the energy resolution for the 2−jet event sample. The linear fit will also yield a correction that can be applied to the $\geq$ 3−jet event energy resolutions in order to be consistent with the 2−jet events [44]. Due to time limitations this correction was not implemented in this analysis.

One limitation of this analysis is the limited event sample caused by the strict topological constraints. Requiring the Tag jet to be restricted to one region of the barrel calorimeter significantly reduces the amount of available statistics. The "matrix" method is another technique that is used to extract calibration factors for

regions of the calorimeter [49]. The matrix method however does not define Tag and Probe jets but rather matches jets from the left ($\eta < 0$) side of the detector to the right ($\eta > 0$) side. The challenge of using this method is that it is much more complicated and not as straightforward to implement.

For future work, this di-jet balance study should be repeated with more data collected by the ATLAS detector. With more data, the jet energy scale for the forward calorimeters can be improved upon and extended to higher p_T values. All three terms in the parametrization of the jet energy resolution can potentially also be determined more accurately as more data is analyzed. When enough data is taken the di-jet balance technique should be applied with the Tag and Probe jets both within the forward calorimeter region. As the luminosity of the proton beams is increased over time, the effect of pileup and underlying events on the jet energy scale and resolution of the forward calorimeters should be studied as well.

Appendix A

This section will present the asymmetry distributions along with their respective Gaussian fits used for the barrel cross-check and determining the jet energy scale and resolution for the forward calorimeters. The chi-square per number of degrees of freedom (χ^2/ndf), constant (p_0), mean (p_1) and standard deviation (p_2) of the Gaussian fits defined by Equation 4.6, as well as the total number of entries are given on each asymmetry distribution.

Figures 6–1 and 6–2 depict the asymmetry distributions of every p_T^{Ave} bin for the 2−jet and $\geq$ 3−jet events respectively, used to verify that the chosen reference region $0.1 < |\eta| < 0.8$ was well calibrated as discussed in Section 5.1. Figures 6–3 and 6–4 show the asymmetry distributions of every p_T^{Tag} bin for the 2−jet and $\geq$ 3−jet events respectively, used to determine the calibration factors and jet energy resolution of the chosen probe region $3.6 < |\eta| < 4.4$ as discussed in Sections 5.2 and 5.4. The asymmetry distributions in Figures 6–5 and 6–6 are of every p_T^{Tag} bin for the 2−jet and $\geq$ 3−jet events respectively, after the jets in the probe region were corrected with the calibration factors listed in Table 5–1.

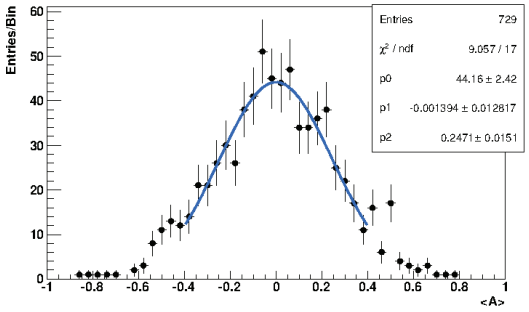

(a) 20-40 GeV/c

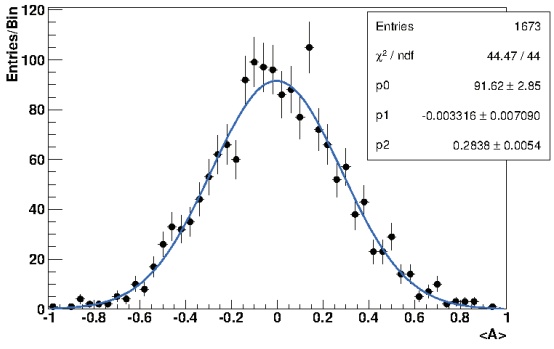

(b) 40-50 GeV/c

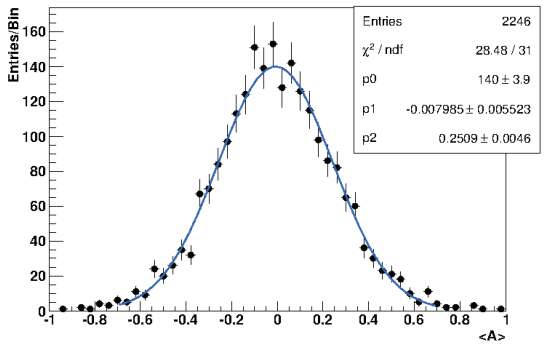

(c) 50-60 GeV/c

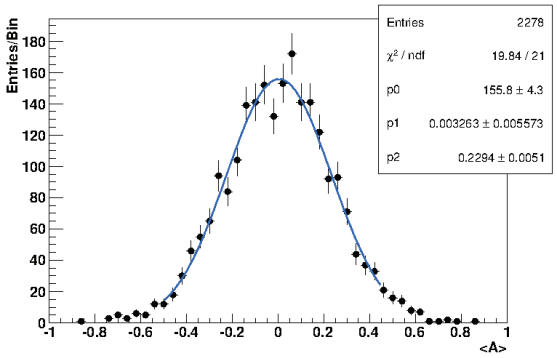

(d) 60-70 GeV/c

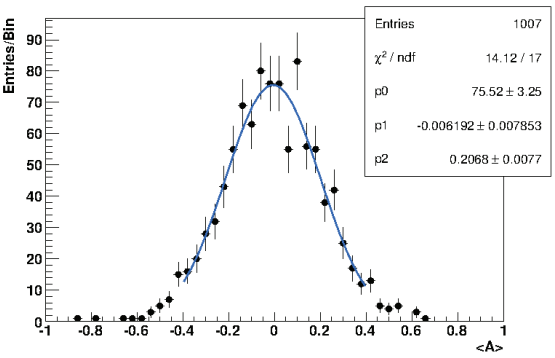

(e) 70-80 GeV/c

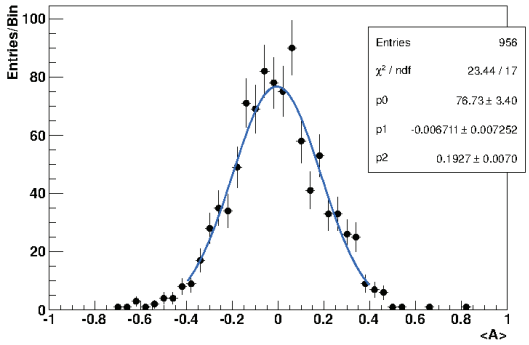

(f) 80-110 GeV/c

Figure 6–1: The asymmetry distributions for every p_T^{Ave} bin of the 2−jet events with the Tag and Probe jets both in the reference region $0.1 < |\eta| < 0.8$. Vertical error bars are purely statistical. All events have passed the selection cuts outlined in Section 4.2.1.

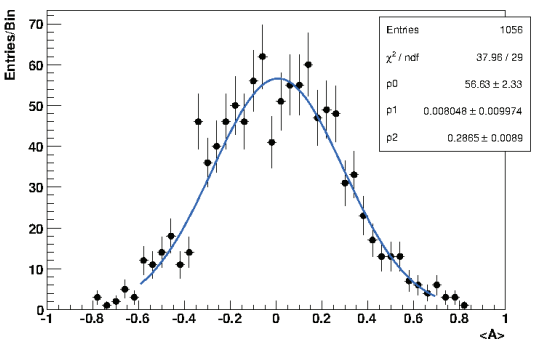

(a) 50-60 GeV/c

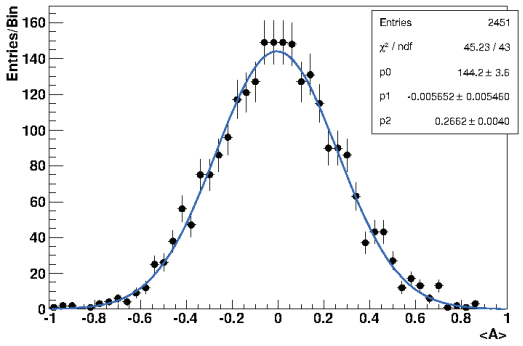

(b) 60-70 GeV/c

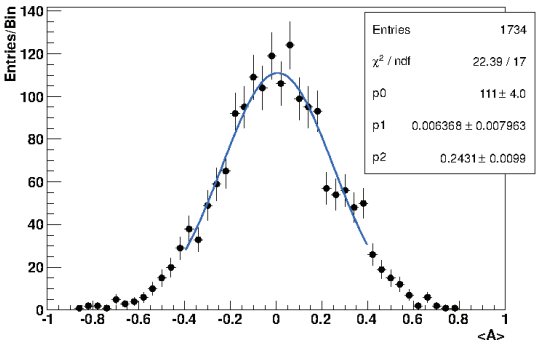

(c) 70-80 GeV/c

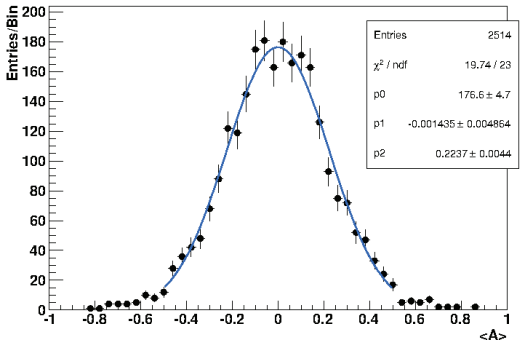

(d) 80-110 GeV/c

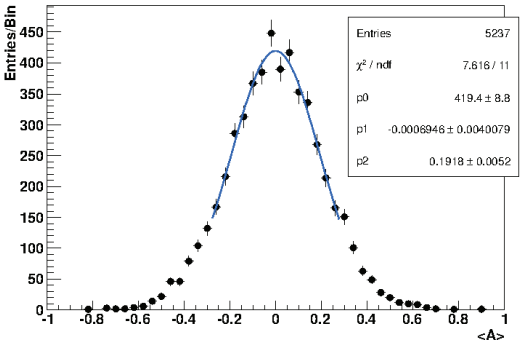

(e) 110-160 GeV/c

Figure 6–2: The asymmetry distributions for every p_T^{Ave} bin of the $\geq 3-$jet events with the Tag and Probe jets both in the reference region $0.1 < |\eta| < 0.8$. Vertical error bars are purely statistical. All events have passed the selection cuts outlined in Section 4.2.1.

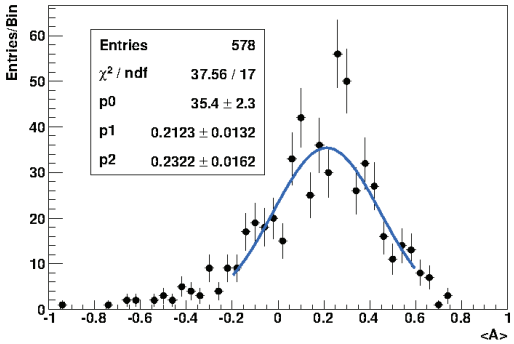

(a) 20-40 GeV/c

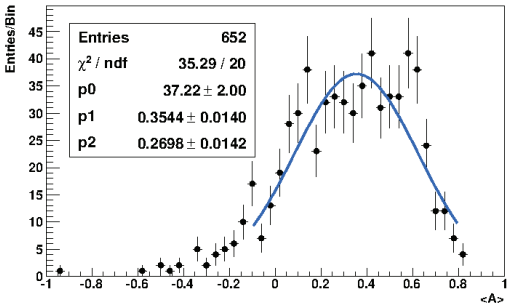

(b) 40-50 GeV/c

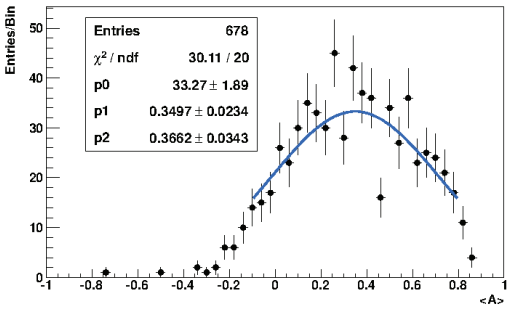

(c) 50-60 GeV/c

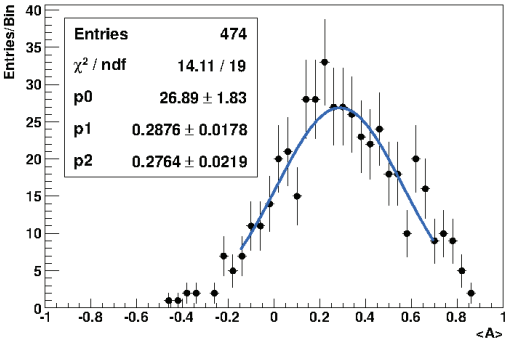

(d) 60-70 GeV/c

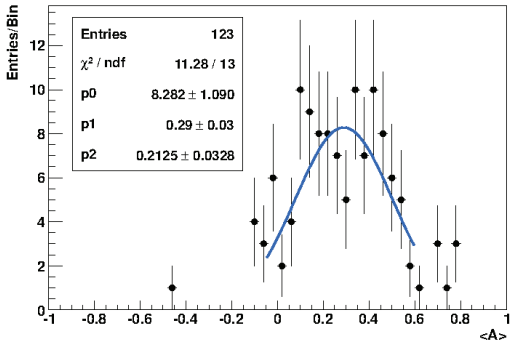

(e) 70-80 GeV/c

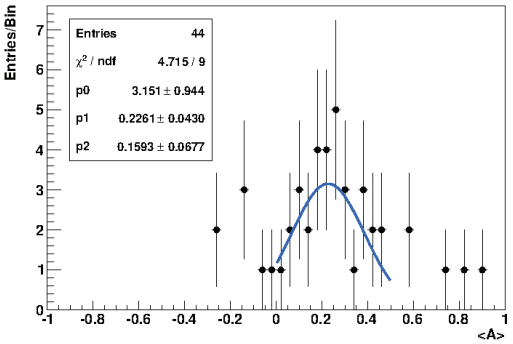

(f) 80-110 GeV/c

Figure 6–3: The asymmetry distributions for every p_T^{Tag} bin of the uncorrected 2−jet events with the Tag jet in the reference region $0.1 < |\eta| < 0.8$ and the Probe jet in the probe region $3.6 < |\eta| < 4.4$. Vertical error bars are purely statistical. All events have passed the selection cuts outlined in Section 4.2.1.

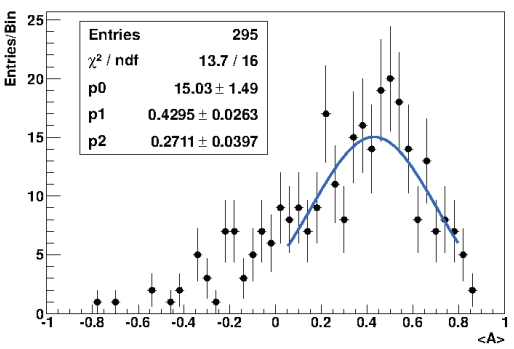

(a) 50-60 GeV/c

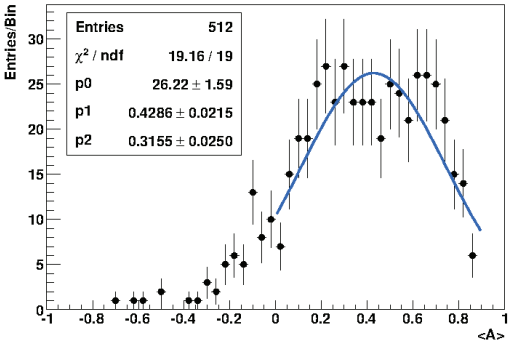

(b) 60-70 GeV/c

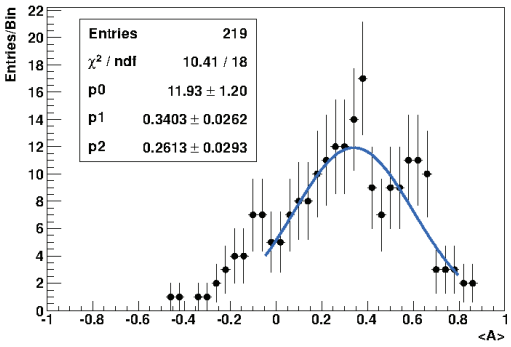

(c) 70-80 GeV/c

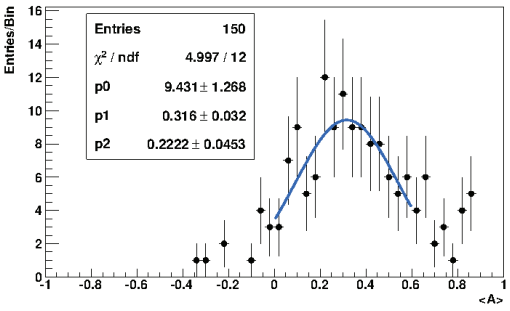

(d) 80-110 GeV/c

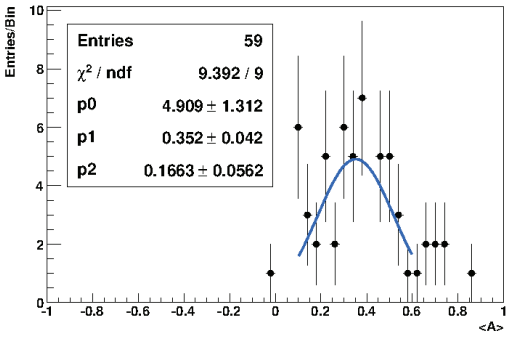

(e) 110-160 GeV/c

Figure 6–4: The asymmetry distributions for every p_T^{Tag} bin of the uncorrected ≥ 3-jet events with the Tag jet in the reference region $0.1 < |\eta| < 0.8$ and the Probe jet in the probe region $3.6 < |\eta| < 4.4$. Vertical error bars are purely statistical. All events have passed the selection cuts outlined in Section 4.2.1.

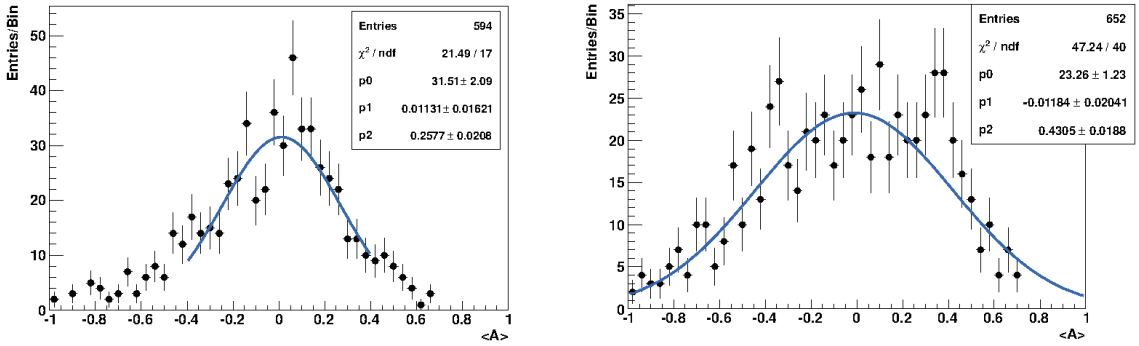

(a) 20-40 GeV/c

(b) 40-50 GeV/c

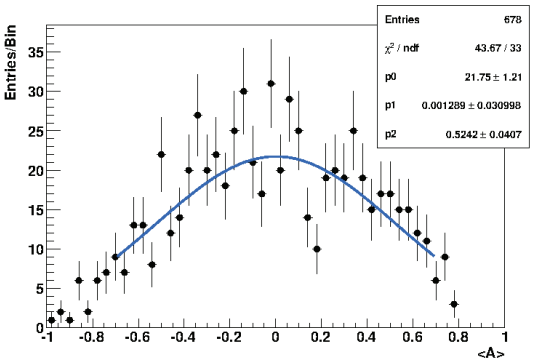

(c) 50-60 GeV/c

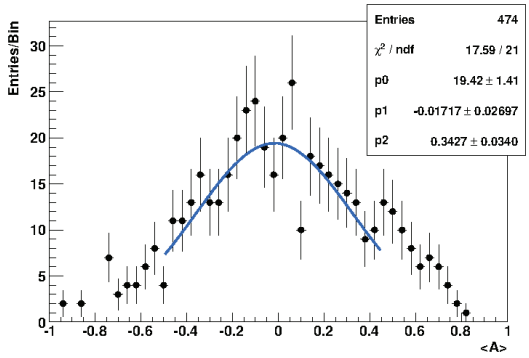

(d) 60-70 GeV/c

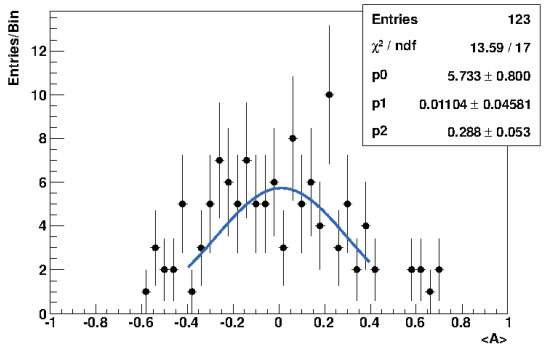

(e) 70-80 GeV/c

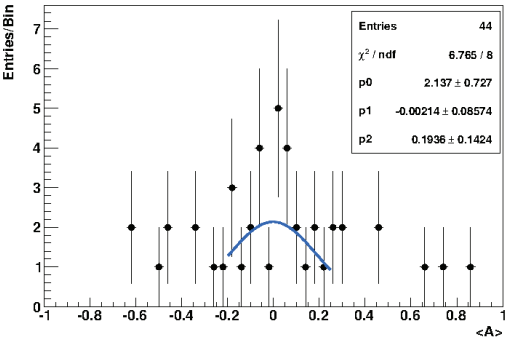

(f) 80-110 GeV/c

Figure 6–5: The asymmetry distributions for every p_T^{Tag} bin of the corrected 2−jet events with the Tag jet in the reference region $0.1 < |\eta| < 0.8$ and the Probe jet in the probe region $3.6 < |\eta| < 4.4$. Vertical error bars are purely statistical. All events have passed the selection cuts outlined in Section 4.2.1.

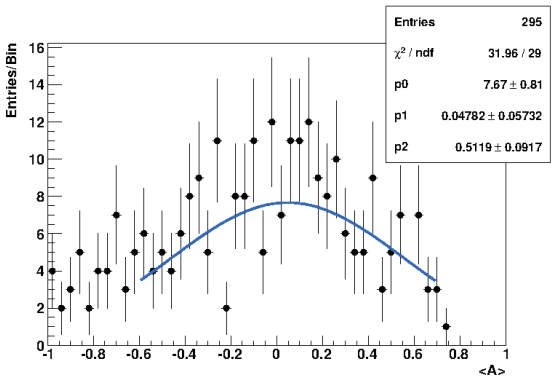

(a) 50-60 GeV/c

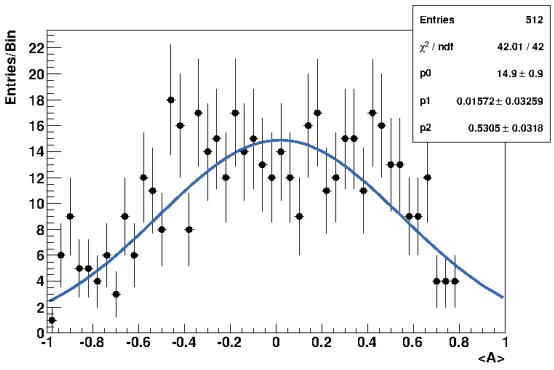

(b) 60-70 GeV/c

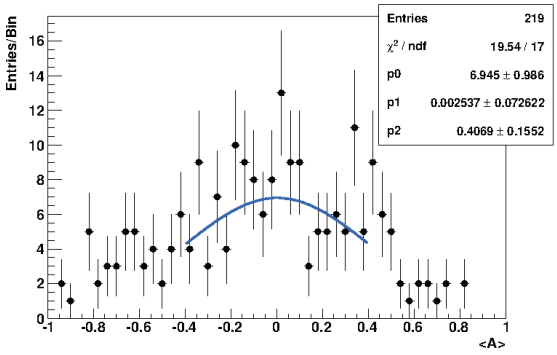

(c) 70-80 GeV/c

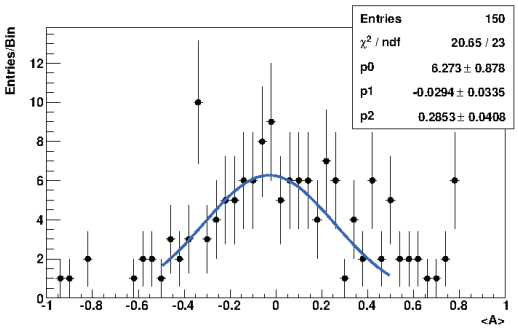

(d) 80-110 GeV/c

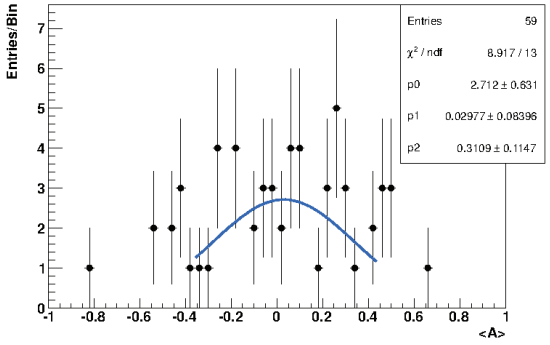

(e) 110-160 GeV/c

Figure 6–6: The asymmetry distributions for every p_T^{Tag} bin of the corrected $\geq$ 3-jet events with the Tag jet in the reference region $0.1 < |\eta| < 0.8$ and the Probe jet in the probe region $3.6 < |\eta| < 4.4$. Vertical error bars are purely statistical. All events have passed the selection cuts outlined in Section 4.2.1.

References

[1] ATLAS Collaboration, ATLAS JER Provider, ATLAS Internal Communication, 2011.

[2] Sabrina Sacerdoti, "Jet Energy Resolution for 2011 -R17 and MC11a", ATLAS Internal presentation, ATLAS Jet Calibration and Resolution Meeting, February 2012.

[3] John R. Taylor, *An Introduction to Error Analysis: The Study of Uncertainties in Physical Measurements*, 2^{nd} edition, University Science Books, Sausaulito, California, 1997.

[4] A. Artamonov, et al., "The ATLAS Forward Calorimeter", JINST 3: P02010, 2008.

[5] S. Dodelson, *Modern Cosmology*, Academic Press, 2003.

[6] S. F. Novaes, "Standard Model: An Introduction", Ariv hep-ph/0001283, 2000.

[7] ATLAS Collaboration, "The ATLAS Experiment at the CERN Large Hadron Collider", JINST 3: S08003, 2008.

[8] S. Weinberg, "A Model of Leptons", Phys. Rev. Lett. 19: p1264-1266, 1967.

[9] The Elementary Particles Included in the Standard Model, http://en.wikipedia.org/wiki/File:Standard Model of Elementary Particles.svg, 2006.

[10] K. Nakamura et al., *Particle Data Group*, J. Phys. G 37, 075021 (2010) and 2011 partial update for the 2012 edition.

[11] The Interactions between the Elementary Particles of the Standard Model, http://en.wikipedia.org/wiki/File:Interactions.png, 2008.

[12] Dag Gillberg, "A Study of Jet Response in the D0 Calorimeters", Master's Thesis, Lund Institute of Technology, 2004.

[13] B. R. Martin & G. Shaw, *Particle Physics*, 3rd Edition, John Wiley & Sons Ltd, 2009.

[14] M.J. Berger & S.M. Seltzer, "Tables of Energy Losses and Ranges of Electrons and Positrons," National Aeronautics and Space Administration Report NASA-SP-3012 (Washington DC 1964).

[15] W. R. Hendee, *Medical Radiation Physics: Roentgenology, Nuclear Medicine & Ultrasound*, 2nd, Year Book Medical Publishers, Chicago, 1979.

[16] Richard Wigmans, "Advances in Hadron Calorimetry", Ann. Rev. Nucl. Part. Sci. 41: 133, 1991.

[17] Pete Watson, "Performance of the Jet Energy Calibration at ATLAS using pT Balance in Z + Jet Events", Master's thesis, McGill University, 2010. Master's thesis.

[18] ATLAS Collaboration, "Expected Performance of the ATLAS Experiment: Detector, Trigger and Physics", ArXiv:0901.0512v4 [hep-ex] (CERN-OPEN-2008-020), 2009.

[19] The LHC Accelerator Complex, http://public.web.cern.ch/public/en/research/AccelComplex-en.html, 2012.

[20] V. Shiltsev, "The Story of the Tevatron Accelerators: Accelerator Science and Technology Breakthroughs, Acheivements and Lessons", Mod. Phys. Lett. A27: 1230001, 2012.

[21] K. Schindl, "The Injector Chain For The LHC", CERN-OPEN-99-52, 1999.

[22] Full ATLAS Detector Image, http://www.atlas.ch/photos/atlas_photos/selected-photos/full-detector/0803012_01-A4-at-144-dpi.jpg, 2012.

[23] Cheuk-Yin Wong, *Introduction to High-Energy Heavy-Ion Collisions*, World Scientific Publishing Co. Pte. Ltd., 1994.

[24] Marjorie D. Shapiro and James L. Siegrist, "Hadron Collider Physics", Annu. Rev. Nucl. Part. Sci. 41: p97-132, 1991.

[25] ATLAS Collaboration, "ATLAS Detector and Physics Performance Technical Design Report", ATLAS-TDR-014 (CERN-LDCC-99-014), 1999.

[26] ATLAS Inner Detector Image, http://www.atlas.ch/photos/atlas_photos/selected-photos/inner-detector/combined/0803014_01-A4-at-144-dpi.jpg, 2012.

[27] A. Andronic and J.P. Wessels, "Transition Radiation Detectors", ArXiv:1111.4188v1 [physics.ins-det], 2011.

[28] E. Abat et al., "The ATLAS Transition Radiation Tracker (TRT) proportional drift tube: design and performance", JINST 3 P02013, 2008.

[29] Katherine Woods, "Energy resolution on trigger jets in the ATLAS experiment at the Large Hadron Collider", Master's thesis, McGill University, 2011.

[30] ATLAS Calorimeter System Image, http://www.atlas.ch/photos/atlas_photos/selected-photos/calorimeters/combined-barrel/0803015_01-A4-at-144-dpi.jpg, 2012.

[31] James E. Brau, John A. Jaros, and Hong Ma, "Advances in Calorimetry", Annu. Rev. Nucl. Part. Sci. 60:Annu. Rev. Nucl. Part. Sci. 60:615-644, 2010. .

[32] ATLAS Muon Spectrometer Image, http://www.atlas.ch/photos/atlas_photos/selected-photos/muon-chambers/combined/0803017_01-A4-at-144-dpi.jpg, 2012.

[33] Rainer Stamen, "The ATLAS Trigger", Universität Mainz, http://pi.physik.uni-bonn.de/teilchenseminar/teilchenseminar0506/stamen.pdf, 2005. .

[34] L. Tompkins, "Performance of the ATLAS Minimum Bias Trigger in $p-p$ collisions at the LHC", ArXiv:1009.6133v1 (ATL-DAQ-PROC-2010-033), 2010.

[35] ATLAS Collaboration, "Charged particle multiplicities in pp interactions for track $p_T > 100$ MeV at $\sqrt{s} = 0.9$ and 7 TeV measured with the ATLAS detector at the LHC, ATL-CONF-2010-046, 2010.

[36] P. Bolzoni, F. Maltoni, S. Moch, and M. Zaro, "Vector boson fusion at next-to-next-to-leading order in QCD: Standard model Higgs boson and beyond", Phys. Rev. D, 85:035002, 2012.

[37] Steven M. Kurtz, editor, *PEEK Biomaterials Handbook*, Elsevier Inc., 1^{st} edition, 2011.

[38] ATLAS Collaboration, G. Aad et al., "Performance of the ATLAS detector using first collision data", JHEP 09: 056, 2010.

[39] ATLAS Collaboration, "In-situ pseudorapidity intercalibration to evaluate jet energy scale uncertainty and calorimeter performance in the forward region", ATLAS-CONF-2010-055, 2010.

[40] Gerald C. Blazey, et al., "Run II Jet Physics", ArXiv:hep-ex/0005012v2, 2000.

[41] ATLAS Collaboration, "Jet energy scale and its systematic uncertainty in proton-proton collisions at $\sqrt{s}$ = 7 TeV with ATLAS 2010 data", ATLAS-CONF-2011-032, 2011.

[42] The CMS Collaboration, "The Determination of Relative jet energy scale at CMS from Dijet Balancing", CMS PAS JME-08-003, 2009.

[43] Doug Schouten, "In Situ Measurements of the Jet Energy Scale in ATLAS", Journal of Physics: Conference Series 323 012003, 2009.

[44] ATLAS Collaboration, "Jet Energy Resolution and Selection Efficiency Relative to Track Jets from In-situ Techniques with the ATLAS Detector Using Proton-Proton Collisions at a Center of Mass Energy $\sqrt{s}$= 7 TeV", ATLAS-CONF-2010-54, 2010.

[45] ATLAS Collaboration, "Performance of the ATLAS Jet Trigger in the Early $\sqrt{s} = 7$ TeV Data", ATLAS-CONF-2010-094, 2010.

[46] ATLAS Collaboration, "Performance of the ATLAS Trigger System in 2010", Eur. Phys. J. C, 72: 1849, 2012.

[47] ATLAS Collaboration, "Performance of the Minimum Bias Trigger in p-p Collisions at $\sqrt{s} = 7$ TeV", ATLAS-CONF-2010-068, 2010.

[48] ATLAS Collaboration, "Data-Quality Requirements and Event Cleaning for Jets and Missing Transverse Energy Reconstruction with the ATLAS Detector in Proton-Proton Collisions at a Center-of-Mass Energy of $\sqrt{s} = 7$ TeV", ATLAS-CONF-2010-038, 2010.

[49] ATLAS Collaboration, "In-situ pseudorapidity intercalibration for evaluation of jet energy scale uncertainty using dijet events in proton-proton collisions at $\sqrt{s}$ = 7 TeV", ATLAS-CONF-2011-014, 2011.